Geophysical Journal International

Helmholtz surface wave tomography for isotropic and azimuthally anisotropic structure

Journal:	*Geophysical Journal International*
Manuscript ID:	Draft
Manuscript Type:	Research Paper
Date Submitted by the Author:	n/a
Complete List of Authors:	Lin, Fan-Chi; University of Colorado at Boulder, Physics Ritzwoller, Michael; University of Colorado at Boulder, Physics
Keywords:	Seismic tomography < SEISMOLOGY, Surface waves and free oscillations < SEISMOLOGY, Wave propagation < SEISMOLOGY, Seismic anisotropy < SEISMOLOGY

For Review Only

SCHOLARONE™
Manuscripts

Helmholtz surface wave tomography for isotropic and azimuthally anisotropic structure

Fan-Chi Lin & Michael H. Ritzwoller
Center for Imaging the Earth's Interior, Department of Physics, University of Colorado at Boulder, Boulder, CO 80309-0390 USA (**fan-chi.lin@colorado.edu**)

Abstract

The growth of the Earthscope/USArray Transportable Array (TA) has prompted the development of new methods in surface wave tomography that track phase fronts across the array and map the travel time field for each earthquake or for each station from ambient noise. Directionally-dependent phase velocities are determined locally by measuring the gradient of the observed travel time field without the performance of a formal inversion. This method is based on the eikonal equation and is, therefore, referred to as "eikonal tomography". Eikonal tomography is a bent-ray theoretic method, but does not account for finite frequency effects such as wave interference, wavefront healing, or backward scattering. This shortcoming potentially may lead to both systematic bias and random error in the phase velocity measurements, which would be particularly important at the longer periods studied with earthquakes. It is shown here that eikonal tomography can be improved by using amplitude measurements to construct a geographically localized correction via the Helmholtz equation. This procedure should be thought of as a finite-frequency correction that does not require the construction of finite-frequency kernels and is referred to as "Helmholtz tomography". We demonstrate the method with Rayleigh wave measurements following earthquakes between periods of 30 and 100 sec in the western US using data from the TA. With Helmholtz tomography at long periods (>50 sec): (1) resolution of small-scale isotropic structures, which correspond to known geological features, is improved, (2) uncertainties in the isotropic phase velocity maps are reduced, (3) the directionally dependent phase velocity measurements are less scattered, (4) spurious 1-psi azimuthal anisotropy near significant isotropic structural contrasts is reduced, and (5) estimates of 2-psi anisotropy are better correlated across periods.

For Peer Review

1. Introduction

Lin et al. (2009, 2011) presented a new surface wave tomography method that was applied to earthquake data and ambient noise cross-correlations recorded by the EarthScope/USArray Transportable Array across the western US (Fig. 1). For each earthquake or station in the context of ambient noise, the method first empirically tracks the propagation of a phase front across the array to determine the phase travel time map and then computes the gradient across each map to estimate the phase velocity at each location. The theoretical justification for this method is based on the eikonal equation (eq. (1)) and the method is, therefore, referred to as eikonal tomography. With multiple earthquakes or multiple stations for ambient noise, the repeated measurements at a single location are summarized statistically to estimate both the isotropic and azimuthally anisotropic components of phase velocity with attendant uncertainties. Similar approaches have been taken by Pollitz (2008) and Liang & Langston (2009) for earthquake data. In contrast with traditional tomographic methods (e.g. Trampert & Woodhouse 1996; Ekstrom et al. 1997; Barmin et al. 2001), the inverse operator of eikonal tomography is simply the spatial gradient applied to the phase travel time map, which is a purely local operator that does not depend on constructing the forward operator. No formal inversion is performed in this method, therefore, which adds to the method's simplicity and the speed of its application. The localized nature of the "inversion" also allows for direct point-by-point inspection of the results, which may be expressed as plots of azimuthally dependent phase velocities as Lin et al. (2009, 2011) illustrate.

The purpose of the current paper is to discuss the limitations of eikonal tomography and to present the means to move beyond it. The basis for eikonal tomography is the eikonal equation:

$$\frac{\hat{k}_i(\mathbf{r})}{c'_i(\mathbf{r})} \cong \nabla \tau_i(\mathbf{r}) \qquad (1)$$

which can be derived from the solution to the 2D Helmholtz wave equation (e.g., Wielandt 1993), by ignoring the effect of the term in the Laplacian of the amplitude field:

$$\frac{1}{c_i(\mathbf{r})^2} = \left|\nabla \tau_i(\mathbf{r})\right|^2 - \frac{\nabla^2 A_i(\mathbf{r})}{A_i(\mathbf{r})\omega^2} \qquad (2)$$

where i is the earthquake index, $\hat{k}$ is the direction of wave propagation, τ is the phase travel time, A is the wave amplitude, $\mathbf{r}$ is position, and ω is the angular frequency. The phase velocites c' and c are explicitly contrasted here. We refer to c' as the "apparent" (sometimes referred to as the "dynamic") phase velocity and c as the "corrected" phase velocity (sometimes referred to as "structural" phase velocity). The eikonal equation (eq. (1)) is only approximately accurate and the apparent and corrected phase velocities will be approximately equal ($c' \cong c$) when the amplitude varies sufficiently smoothly or the frequency is high enough so that the second term on the right of eq. (2) will be much smaller than the first term. We refer to the term in eq. (2) involving the Laplacian of the amplitude (without the negative sign) as the amplitude correction

For Peer Review

term for the Eikonal equation. This term defines the difference between the apparent and corrected phase velocities. In the following, we will refer to results based on eqs. (1) and (2) as the apparent and corrected phase velocity maps, respectively, which should be distinguished from the intrinsic phase velocity for the real earth.

Eikonal tomography (based on eq. (1)) is a geometrical ray theoretic method. Several theoretical and numerical studies (e.g., Wielandt 1993, Friederich et al. 2000, Bodin & Maupin 2008) have shown that when the wavelength is comparable to or larger than the dimension of a structural anomaly, ignoring the amplitude correction term in eq. (2) can cause underestimation of the anomaly amplitude and the introduction of isotropic bias into inferred azimuthal anisotropy. While Lin et al. (2009) presented eikonal tomography through applications to ambient noise cross-correlation measurements (Bensen et al. 2007; Lin et al. 2008), the method was extended to earthquake data by Lin et al. (2011) to constrain azimuthal anisotropy up to ~50 sec period. Lin & Ritzwoller (2011) demonstrated isotropic bias in azimuthal anisotropy measurements above ~50 sec period and showed that the observed bias increases with period and can be explained as off-ray sensitivity or a finite frequency effect. In particular, they identified the existence of a strong non-physical 1-psi component of the azimuthal anisotropy measurements (360 degree periodicity), which results from back-scattering in the neighborhood of stations. Similar bias is also observed for ambient noise applications at long periods (Ritzwoller et al. 2011).

Accurately estimating long period (>50 sec) phase velocity maps is desired to be able to resolve upper mantle structure. Unlike ambient noise measurements where the amplitude information is degraded or obscured during temporal and frequency normalization (e.g. Bensen et al. 2007; Lin et al. 2007), the amplitude of earthquake signals can be measured directly along with phase travel times. This provides the possibility to compute the amplitude term in the Helmholtz equation (e.g., Pollitz & Snoke 2010). Whether earthquake amplitudes provide a meaningful and accurate correction to Eikonal tomography is the motivation for this study.

Amplitude measurements have been used in both global (e.g., Dalton & Ekstrom 2006) and regional (e.g. Yang & Forsyth 2006; Yang et al. 2008; Pollitz 2008) tomography to constrain surface wave phase velocity structures. In the regional methods, to achieve the high resolution desired, phase and amplitude measurements across an array are used jointly to invert for the properties of the incoming waves along with the structural variation. To stabilize the inversion, the incoming waves are often assumed to be the superposition of a few basis functions such as plane waves. Analytical finite frequency kernels (e.g. Zhou et al. 2004) are used in the inversion to account for the waveform complexity due to internal structural heterogeneities. Recently, Pollitz & Snoke (2010) demonstrated a new approach that determines phase velocity structures and wave properties locally through a sub-array configuration. When the sub-array is contained within a small region, a homogenous phase velocity structure can then be assumed and hence finite frequency kernels are not required. In essence, this local inversion approach is very similar to the idea of eikonal tomography (Lin et al. 2009) and the Helmholtz tomography described in

For Peer Review

this study although no assumption about the form of the incoming wave is made here. Due to the similarity of theory and approach involved, we expect our results to be largely consistent with the results presented by Pollitz & Snoke (2010). The focus here, however, is to study the effect of the amplitude correction on the phase velocity measurements and to evaluate the importance of the finite frequency effect on both isotropic and azimuthally anisotropic results.

In this study, we apply both phase front tracking and amplitude measurement to Rayleigh wave tomography between 30 and 100 sec period across the USArray in the western US (Fig. 1) based on earthquake data (Fig. 2a). For each earthquake, the resulting phase travel time and amplitude maps are used to estimate the apparent (c') and corrected (c) phase velocity maps based on eqs. (1) and (2), respectively. We show that amplitude measurements are strongly correlated with phase bias and can be used to account for finite frequency effects. We present several clear lines of evidence that Helmholtz tomography outperforms eikonal tomography, particularly at long periods (> 50s). This evidence includes (1) better resolved small-scale isotropic anomalies, which correspond to known geological features, (2) smaller uncertainties in the isotropic phase speed maps, (3) less scattered directionally dependent phase velocity measurements, (4) reduced amplitude of the spurious 1-psi component of azimuthal anisotropy, and (5) better correlation between the observed 2-psi (180 degree periodicity) azimuthal anisotropy between different periods.

2. Methods

To demonstrate the Helmholtz tomography method we use all USArray stations (Figure 1) and more than 700 earthquakes (Figure 2a) with Ms > 5.0 that occurred between January 1st, 2006 and April 11th, 2010. For each earthquake and wave period, we apply automated frequency-time analysis (FTAN; e.g. Levshin & Ritzwoller 2001; Lin et al. 2007) to measure both the phase travel time and the wave amplitude for Rayleigh wave signals emitted from these earthquakes across the array. We discard all measurements with signal-to-noise ratio (SNR; Lin et al. 2008) less than 10. Due to the degradation of data quality and SNR at long periods, the number of earthquakes used in this study decreases with period (Figure 2b).

2.1 Phase front tracking and amplitude measurement

Before estimating the phase velocity based on eqs. (1) and (2) with the spatial gradient and Laplacian operators, we first construct the phase travel time and amplitude maps for each earthquake. For phase travel time measurements from the same earthquake, we correct the relative 2π ambiguity for all measurements before further analysis. The correction is made sequentially in an order determined from the distance between each station to the center of the array (from short to long distances). To resolve the 2π ambiguity at a target station, the average phase speed (phase travel time divided by the great circle distance) for the nearest corrected station is used as the reference to predict the phase travel time at the target station. The observed phase travel time at the target station is allowed to change within the interval of one wave period

For Peer Review

until the misfit to the predicted travel time is minimized. We remove all measurements with a misfit larger than 6 seconds. Only earthquakes with valid measurements from at least 50 stations across the array are used for further analysis.

We follow the method described by Lin et al. (2009) to construct both the phase travel time (τ) and amplitude (A) maps based on a minimum curvature surface fitting technique (Smith & Wessel 1990). All available phase travel time and amplitude measurements are interpolated onto a 0.2° × 0.2° grid based on the surface fitting method. As additional quality control, stations at where the absolute phase travel time curvature is larger than 0.005 s^2/km^2 or amplitude curvature is larger than $A\omega^2/c_0^2$ are discarded before constructing the final travel time and amplitude maps. The reference velocity c_0 is set to 4 km/s in the amplitude selection criterion. Figure 3 shows examples of the resulting 60 sec Rayleigh wave phase travel time and amplitude maps based on two earthquakes identified by green circles in Fig. 2a.

As demonstrated in Figure 3, the observed phase and amplitude fields are significantly different, which underscores the challenge of using amplitude information in a tomographic inversion. While the phase travel time varies smoothly and monotonically in the direction of wave propagation, both large and small-scale variations are observed in the amplitude maps both in the direction of wave propagation and transverse to it. For example, a prominent low amplitude stripe is observed in Figure 3b, which is probably caused by wave-wave interference produced by structural variations outside the array. Note, however, that kinks in the phase travel time contours for this event (Fig. 3a) probably result from the same structural cause as the amplitude stripes (Fig. 3b). Some amplitude maps are much smoother than others (e.g., Fig. 3d), which probably reflects wave propagation conditions outside the array.

2.2 Event-specific apparent and corrected phase velocities

With the phase travel time and amplitude maps, we compute the gradient of the phase travel time field and the Laplacian of the amplitude field to estimate the apparent and corrected phase velocity based on eqs. (1) and (2), respectively. While the gradient varies smoothly for a map computed with minimum curvature surface fitting, the Laplacian is not necessarily well behaved. To ameliorate this technical difficulty and provide a smooth estimate of the Laplacian, we first calculate the first spatial derivative in the longitudinal and latitudinal directions at all station locations where amplitude measurements are available. We then re-apply the surface fitting method to determine the first spatial derivative maps in the longitudinal and latitudinal directions for the whole region of the active array. The second spatial derivatives are then calculated, but they now provide a smoothly varying estimate of the Laplacian. It must be acknowledged that the methods we apply here to fit the travel time and amplitude surfaces and to calculate the Laplacian of the amplitude field are not unique and are probably not optimal. In particular, the Laplacian of the amplitude field is probably underestimated for small-scale amplitude variations (relative to station spacing) based on minimum curvature surface fitting (see section 5.3).

For Peer Review

To demonstrate the ability of the amplitude measurements to reduce the apparent bias in the travel time (or phase) measurements, Figure 4 presents examples of an apparent phase velocity map defined from eq. (1), the amplitude correction map ($\nabla^2 A / \omega^2 A$) defined by eq. (2), and the corrected phase velocity map also defined by eq. (2). These results are all calculated from the phase travel time and amplitude maps shown in Fig. 3. Clear correlations are observed between the apparent velocity anomalies and the amplitude correction surface for the 2009 Kuril Islands earthquake (Fig. 4a-b). Both maps show a prominent stripe that presents as an apparent low velocity trough in Figure 4a and a high amplitude ridge in the Laplacian surface in Figure 4b. This correlation is evidence that the amplitude correction term can be used to suppress spurious apparent phase velocity signals. In fact, the striped interference pattern is no longer observed in the corrected phase velocity map (Fig. 4c) and various prominent structural anomalies can now be seen including the slow anomalies of the Yellowstone/Snake River Plain hot spot track and the southern Rocky Mountains and the fast anomaly in southwestern Wyoming. The apparent phase velocity and the amplitude correction maps for the 2007 Easter Island earthquake (Fig. 4d-e), on the other hand, display a weaker correlation which suggests that wave interference is not as severe and the observed apparent phase velocity better reflects regional-scale structures. This is consistent with the difference in magnitude between the amplitude correction term shown in Figures 4b and 4e. Nevertheless, the fast anomalies of the subducted Juan de Fuca Plate and the Isabella anomaly near the Sierras in southern California are better resolved in the corrected phase velocity map (Fig. 4f).

3. Isotropic Phase Velocity Maps

We follow the methods described by Lin et al. (2009) to statistically summarize measurements based on a large number of earthquakes for each spatial location. Figure 5 shows example distributions of apparent and corrected phase velocity measurements for the 60 sec Rayleigh wave compute at two locations (stars in Fig. 1). The distributions of the corrected phase velocities in general are more concentrated (Fig. 5c-d) than the apparent phase velocities (Fig. 5a-b) likely reflecting the reduction of random phase bias with the amplitude correction. We calculate both the mean and the standard deviation of the mean of all measurements at each location to estimate the isotropic phase velocity and its uncertainty at each location.

The final apparent and corrected isotropic phase velocity maps in the western US for the 60 sec Rayleigh wave and their uncertainties are shown in Figure 6a-b and Figure 7. On average, the corrected phase velocity map displays larger velocity contrasts for small-scale anomalies. These anomalies are correlated with known geological features (Fig. 6c) such as the fast anomalies of the Isabella anomaly in southern California and the Colorado Plateau and the slow anomalies of the Clear Lake volcanic field in northern California, the Long Valley Caldera, the Newberry Caldera, and the Yellowstone/Snake River Plain hot spot track, many of which are also observed in body wave tomography (e.g. Schmandt & Humphreys 2010). The observation that the apparent phase velocity map underestimates the amplitude of small-scale anomalies is consistent

For Peer Review

with previous theoretical and numerical studies (e.g. Wielandt 1993, Friederich et al. 2000, Bodin & Maupin 2008).

The difference between the corrected and apparent isotropic velocities is presented in Figure 6c. This difference represents the discrepancy arising from the fundamental theories applied, the eikonal equation versus the Helmholtz equation. This difference is not accounted for in the uncertainty estimates shown in Figure 7, which mostly reflects random fluctuations rather than systematic bias. The corrected isotropic phase velocities based on Helmholtz tomography, in general, have smaller uncertainties than those from eikonal tomography due to the reduction of variations in the measurements (Fig. 7). In both cases, uncertainties grow toward the east because the time of operation of the eastern stations is shorter than for western stations. Fewer earthquakes were analyzed in the eastern than the western part of the region of study.

The isotropic phase velocity maps at two other periods, 40 and 80 sec, are shown in Figure 8. The maps at 80 sec period (Fig. 8d-f) demonstrate clearly the advantage of using Helmholtz tomography to resolve smaller-scale anomalies at long periods. Similar to the result at 60 sec period (Fig. 6), small-scale anomalies are more pronounced and in better agreement with body wave tomography results (e.g. Schmandt & Humphreys 2010). At 40 sec period, on the other hand, the differences between eikonal and Helmholtz tomography are mostly small with the exception of the Isabella anomaly, which is slightly more pronounced in the corrected map.

By applying the amplitude correction term, Helmholtz tomography accounts for both wave interference and wavefront healing effects which probably produce the reduction of random and systematic errors, respectively. Figure 9 summarizes the average uncertainties of the isotropic phase velocity maps based on the two tomography methods and the standard deviation (Std) of the systematic differences between the two isotropic maps across the western US at each period. The isotropic phase velocity structures produced by Helmholtz tomography have smaller uncertainties compared to the result from eikonal tomography (Fig. 9a) due to the reduction of measurement variation. The overall increase of uncertainty with period for both tomography methods (Fig. 9a) probably results from the decrease in the number of earthquakes used at longer periods (Fig 2b). The standard deviation of the systematic differences increases with period and are roughly three times larger at 100 sec period (~33 m/s) than at 30 sec period (~11 m/s) (Fig. 9b). The systematic differences between Helmholtz and eikonal tomography, hence, are clearly due to the finite frequency effects. Helmholtz tomography, which accounts for finite frequency effect, clearly outperforms eikonal tomography in resolving isotropic structures and should be used at least at periods longer than ~50 sec for array configurations similar to the TA.

For Peer Review

4. Anisotropy Maps

For both eikonal and Helmholtz tomography, the gradient of the phase travel time (eq. (1)) provides the approximate local direction of wave propagation for each earthquake. For each location, we follow the method described by Lin et al. (2009) to estimate the phase velocity and its uncertainty within each 20° azimuthal bin based on the mean and the standard deviation of the mean of the measurements taken from all the earthquakes within each bin. A 9-point (3×3 grid with 0.6° separation) averaging scheme is used to reduce small-scale variability in the measurements.

Figure 10 presents examples of the directionally dependent apparent and corrected phase velocity measurements at two locations (stars in Fig. 1) for the 60 sec Rayleigh wave. Based on observations such as those in Figure 10, we find that the principal components of the azimuthal variation of the phase velocity measurements have 180° and 360° periodicities. Therefore, instead of the 180° periodicity in the expected functional form for a weakly anisotropic medium (Smith & Dahlen 1973), we assume that the phase velocity exhibits both a 180° and a 360° periodicity:

$$c(\psi) = c_{iso}\left\{1 + \frac{A_{1psi}}{2}\cos\left(\psi - \varphi_{1psi}\right) + \frac{A_{2psi}}{2}\cos\left[2\left(\psi - \varphi_{2psi}\right)\right]\right\} \quad , \qquad (3)$$

where c_{iso} is the isotropic component of wave speed, ψ is the azimuthal angle measured positive clockwise from north, A_{1psi} and A_{2psi} are the peak-to-peak relative amplitude of 1-psi and 2-psi anisotropy, and φ_{1psi} and φ_{2psi} define the orientation of the anisotropic fast axes for the 1-psi and 2-psi components, respectively. Based on results from eikonal tomography, Lin & Ritzwoller (2011) argued that the 1-psi anisotropy signal, which is nonphysical because it violates the reciprocity principle, probably reflects an inaccuracy in eikonal tomography. In particular, they argued that the 1-psi signal resulted from unmodeled near-station backward scattering. Backward scattering is a finite frequency effect in which the observed apparent phase velocity at a location is sensitive to structures downstream of the recording station in the direction of wave propagation. Near a sharp structural contrast, this results in an apparent 1-psi anisotropy signal in which the fast direction points toward the faster structure. A much more detailed discussion can be found in Lin & Ritzwoller (2011).

In general, the observed directionally dependent phase velocities become less scattered and better fitted by Helmholtz tomography than by eikonal tomography (Fig. 10). This is because of a reduction of directionally dependent bias, which can be caused by consistent wave interference patterns induced by structures outside of the array (e.g. Fig 4a-c). Note that this directionally dependent bias will act as a random scatter for the isotropic velocity measurement. Figure 11a-b summarizes the chi-square misfits of the best fitting curves based on eq. (3) for 60 sec Rayleigh wave measurements at each location based on the two tomography methods. Figure 11c summarizes the average chi-square misfits across the entire western US at each period. The

For Peer Review

corrected phase velocities are better fitted by eq. (3) than the apparent phase velocities in every case, suggesting that the directionally dependent bias is significantly reduced with Helmholtz tomography. This is a feature needed to resolve azimuthal anisotropy robustly.

The estimated 1-psi and 2-psi azimuthal anisotropy patterns (particularly the 1-psi term) also can be significantly different based on the two tomography methods (e.g. Fig. 10). Because the 1-psi signal reflects isotropic bias (Lin and Ritzwoller, 2011), we seek a tomography method that reduces the 1-psi signal. In contrast, the 2-psi signal is more difficult to interpret as it reflects both physical anisotropy and perhaps also bias. Because of this difference in interpretation of the 1-psi and 2-psi signals, we discuss each in turn.

4.1 1-psi anisotropy as indicative of theoretical errors

A summary of the 1-psi component of azimuthal anisotropy for both the apparent and corrected phase velocity measurements across the western US for the 60 sec Rayleigh wave is presented in Figure 12. By comparing with the isotropic velocity structures shown in Figure 6b, the observed 1-psi anisotropy (Fig. 12a-b) can be seen to be clearly correlated with sharp isotropic structural boundaries with fast directions pointing toward the faster isotropic structure. This confirms that the 1-psi signal is a form of isotropic bias in the azimuthal anisotropy measurements (Bodin & Maupin 2008; Lin & Ritzwoller 2011). The strength of the spurious 1-psi signal is significantly reduced in the corrected velocity map (Fig. 12b), however.

To demonstrate the frequency dependence of the 1-psi anisotropy signals, Figure 13 summarizes the 1-psi component of azimuthal anisotropy for the 40 and 80 sec Rayleigh waves. Figure 13e presents the averaged 1-psi amplitude over the entire western US at each period. Overall, the 1-psi anisotropy is clearly more pronounced at long periods, consistent with this spurious signal being a finite frequency effect. Note that the average 1-psi amplitude decreases only slowly toward the short period for both apparent and corrected measurements in Figure 13e, suggesting that the background random measurement errors probably also contribute somewhat to the observed 1-psi signals.

Even with the finite frequency corrections made by Helmholtz tomography, some spurious 1-psi signals remain, particularly at 60 and 80 sec period near the edge of the southwestern Wyoming fast anomaly (Fig. 12b, 13d). Thus, as it is currently effected, Helmholtz tomography remains insufficient to completely remove the effects of sharp isotropic structural boundaries on nearby azimuthally anisotropy measurements with the current station configuration. This inability to completely remove 1-psi anisotropy is discussed further in section 5.2.

4.2 2-psi anisotropy

In contrast with the 1-psi anisotropy, the difference between the apparent and corrected 2-psi azimuthal anisotropy is rather subtle at 60 sec period (Fig. 14a-c). Various notable differences at 60 sec period include regions near northern Oregon, the Yellowstone hot spot, and the southern

For Peer Review

Rocky Mountains where strong isotropic anomalies are present (Fig. 6b). These differences may represent isotropic bias in the apparent phase velocity measurements due to unmodeled finite frequency effects.

Better evidence that Helmholtz tomography is correcting for isotropic bias comes from the period dependence of the differences between the eikonal and Helmholtz tomography methods. Figure 15 summarizes the results of 2-psi anisotropy for the 40 and 80 sec Rayleigh waves and Figure 16a summarizes the standard deviation (Std) of the fast direction differences between the 2-psi anisotropy results of Helmholtz tomography and eikonal tomography at each period. While the 2-psi anisotropy observed from apparent and corrected velocity measurements with eikonal and Helmholtz tomography, respectively, are similar at 40 second (Fig. 15a-c), they are quite different at 80 sec period (Fig. 15d-f). The fact that the differences in the 2-psi fast direction between eikonal and Helmholtz tomography increase with period (Fig. 16a) suggests that this difference is mostly due to finite frequency effects. Lin & Ritzwoller (2011) argue that the 2-psi anisotropy bias in eikonal tomography may be caused by the broad forward scattering sensitivity kernels of the phase travel time measurements. This bias is particularly strong near linear isotropic anomalies where the 2-psi anisotropy fast direction either is aligned or perpendicular to the linear slow or fast anomaly, respectively. This is consistent with the assumption that the observed 2-psi anisotropy at 80 sec period based on eikonal tomography (Fig. 15d) is heavily biased where the fast directions are better aligned with linear slow anomaly structures (Fig. 8e) such as the north-south fast direction near northern Oregon east of Cascades and northeast-southwest fast direction near eastern Idaho within the Snake River Plain.

Another line of reasoning that demonstrates that Helmholtz tomography reduces bias in 2-psi anisotropy comes from the comparison of observed 2-psi anisotropy at different periods. In Figure 16b, we present the vector correlation coefficient (Lin et al. 2011; Lin & Ritzwoller 2011) between the 2-psi fast directions observed at 40 sec period and all other periods. Only locations with observed 2-psi anisotropy amplitude larger than 0.5% are included in the calculation. Considering that Rayleigh waves are most sensitive to uppermost mantle structures for the period range considered here, it is unlikely that the intrinsic 2-psi anisotropy at different periods will be strongly different and uncorrelated. Hence, the fact that the observed 2-psi anisotropy at long periods is correlated better with the result at 40 sec period based on Helmholtz tomography is evidence of less bias in the observations. Using the 80 sec results as an example, the observed 2-psi apparent fast directions based on eikonal tomography (Fig. 15d) are only weakly correlated with the result at 40 sec (Fig. 15a) with a vector correlation coefficient equal to 0.24. In contrast, the vector correlation coefficient is equal to 0.46 for the Helmholtz tomography result (Fig. 15b,e). We compare the results at all periods to 40 sec result because finite frequency bias is expected to be smaller at 40 sec period (Fig. 15a-b).

Although it is difficult to determine the degree of bias in 2-psi anisotropy, our results suggest that finite frequency effects need to be accounted for to obtain unbiased 2-psi anisotropy measurements. As shown in Figure 16a, however, the 2-psi bias due to finite frequency effects is

For Peer Review

probably small below about 50 sec period, but gradually becomes more important at longer periods (>50 sec). This justifies the use of eikonal tomography at short periods (<50 sec) to constrain shallow structures in the crust and uppermost mantle, particularly when the amplitude information is not available such as for ambient noise application (e.g. Ritzwoller et al., 2011; Lin et al. 2011). At long periods (>50 sec), however, the 2-psi anisotropy observed based on Helmholtz tomography better reflects intrinsic anisotropy. Caution should be taken, however, in interpreting the long period results particularly before the 1-psi anisotropy signals can be more completely removed.

5. Technical Discussion

Based on the results shown in foregoing, Helmholtz tomography more accurately accounts for finite frequency effects and provides better estimates of both isotropic and azimuthally anisotropic structures than eikonal tomography, particularly at periods above about 50 sec. In this section we discussed several technical issues that combine to determine and in some cases limit the effectiveness of Helmholtz tomography.

5.1 Detailed comparison between finite frequency bias and the amplitude correction term

The ability to use amplitude measurements to ameliorate finite frequency bias in the apparent phase velocity measurements relies on that the existence of a good correlation between the two. We attempt to quantify this here and investigate circumstances when the amplitude measurements do not remove bias completely.

For each earthquake we compare the apparent bias in corrected slowness squared ($\alpha \equiv \left|\nabla \tau_i(\mathbf{r})\right|^2 - \frac{1}{c_0(\mathbf{r})^2}$) with the amplitude correction term ($\beta \equiv \nabla^2 A_i(\mathbf{r})/(A_i(\mathbf{r})\omega^2)$) defined by eq. (2). In order to minimize the scatter caused by spatial variations in phase speed, we use the isotropic phase velocity speed obtained with Helmholtz tomography (e.g. Fig 6b and 8b,e) to evaluate $c_0(\mathbf{r})$. Based on eq. (2), if $c_0(\mathbf{r})$ accurately reflects the intrinsic phase velocity structure, a linear relationship is expected between the apparent bias (α) and the amplitude correction term (β):

$$\alpha(\beta) = \lambda\beta \qquad (4)$$

In fact, we expect $\alpha \approx \beta$, but introduce a correction factor λ to account for difficulties in estimating either the apparent bias or the amplitude correction term. Theoretically, λ should be equal to 1.

Figure 17 presents an example of the corrected apparent bias (α), the amplitude correction term (β), and their relationship across the wesetern US for the 60 sec Rayleigh wave following the Easter Island earthquake. A good correlation between the apparent bias (α) and the amplitude correction term (β) is observed (correlation coefficient ρ=0.84) with the correction factor

For Peer Review

($\lambda \approx 1.15$) near unity. This suggests that for this earthquake most of the finite frequency bias can be removed with the amplitude correction term based on the Helmholtz equation (eq. (2)).

Going further, Figure 18a presents a histogram of the correlation coefficient (ρ) between the finite frequency bias (α) and the amplitude correction factor (β) and Figure 18b shows a histogram of the correction factor (λ) for all earthquakes at 60 sec period. The vertical axis in each histogram is percentage of all earthquakes. Generally, the correction factor λ is near 1 (average of 1.03) and the correlation between the finite frequency bias and the amplitude correction factor ρ is better than about 0.3 with an average of 0.54. This justifies the use of the Helmholtz equation to suppress finite frequency effects and measurement bias. Nevertheless, there are outlier earthquakes that we seek to understand.

To provide further insight, Figure 18c presents the relationship between ρ and λ for each earthquake. Clear correlation is observed between the correlation coefficient ρ and correction factor λ (Fig. 18c). In particular, the correction factor λ is considerably smaller than the theoretical value of unity when the correlation coefficient is small (ρ<0.3). For earthquakes in which the amplitude correction map is not well correlated with the apparent phase velocity map, the amplitude correction term is not useful to remove apparent phase velocity variations. Earthquakes belonging to this category usually have weak amplitude measurements (Fig. 18d). This degrades the ability of the observed amplitude field to correct the phase measurements.

Unlike low correlation coefficient (ρ<0.3) earthquakes, the events with high correlation coefficients (ρ>0.5) and high correction factors (λ>1.5) are more mysterious. Figure 19 shows an example of such an earthquake for the 60 sec Rayleigh wave. One common characteristic of this type of outlier is that both the apparent phase velocity map (Fig. 19c) and the amplitude correction term (Fig. 19d) display oscillations in the direction of wave propagation. While the apparent phase velocity and amplitude correction variations are highly correlated, the correction factor λ is significantly larger (>1.5; e.g. Fig. 19e) than the theoretical value of unity. Applying the amplitude correction to such an earthquake based on eq. (2), therefore, does not fully remove the apparent oscillatory bias in the phase velocity measurements (Fig. 19f). Because any superposition of fundamental Rayleigh waves should still satisfy the Helmholtz equation (eq. 2), we suspect that the oscillatory pattern is due to interference with another wave type such as a body wave or a higher mode. An understanding of the detailed cause of this phenomenon, however, is beyond the scope of this study.

In practice, we can identify and discard these outlier earthquakes by setting a selection criterion based on the correlation coefficient ρ and correction factor λ. The number of outliers is small, however, and removing them does not have a noticeable effect on the final result. Besides the apparent outliers, Figure 18c also shows that many high correlation coefficient ρ earthquakes have a correction factor λ somewhat larger than unity (but smaller than 1.5). We suspect that this

For Peer Review

is caused by the average underestimation of the Laplacian term, which will also be discussed further in Section 5.3.

5.2 Unmodeled finite frequency effects

In general, velocity measurements based on finite frequency surface waves are affected by wave interference, wavefront healing, and backward scattering. While wave interference is probably event-dependent and predominantly introduces random measurement errors, the effect of wavefront healing and backward scattering is more systematic and is likely to produce bias in observed variables. In general, wavefont healing acts to smear out isotropic velocity anomalies and introduces 2-psi anisotropic bias. Backward scattering, on the other hand, introduces non-physical 1-psi anisotropic signals (Lin & Ritzwoller 2011).

In earlier sections, we presented several lines of evidence that Helmholtz tomography accurately accounts for these finite frequency effects. This evidence included the observation of lower variance in the velocity measurements (reducing the effect of wave interference), better resolution of small scale isotropic structures and 2-psi anisotropy (reducing the effect of wavefront healing), and the overall reduction of 1-psi anisotropy (reducing the effect of backward scattering). Somewhat disappointingly, however, Helmholtz tomography falls short of completely removing the spurious 1-psi signals which we argue are an indicator of the severity of systematic bias in the inversion. The systematic bias in isotropic and 2-psi anisotropic measurements are entangled with intrinsic structural variations and, therefore, are harder to evaluate.

Although removing the 1-psi anisotropic signals is entirely desired and may potentially lead to better resolved structural boundaries, it may require a more precise knowledge of near-field backward scattering sensitivity (sensitivity very close to the receiver). The Helmholtz equation (eq. (2)) used in this study, although finite frequency theory, is an instantaneous frequency equation. Constructing a finite frequency kernel based on the 2D Helmholtz equation can result in strong side lobe oscillation particularly in the backward scattering region (Zhou et al. 2004). Because a finite band-width filter is used in the frequency-time analysis to obtain phase and amplitude measurements at each period, there is an apparent inconsistency between our measurements and the theory employed. It is unclear, however, whether finite band-width finite frequency kernels constructed based on a simple reference model (e.g. Zhou et al. 2004) will be sufficient to provide such information considering that structurals variation can significantly alter the sensitivity kernesl (Lin & Ritzwoller 2010). Numerical studies (Tromp et al. 2005; Tape et al. 2010), on the other hand, may provide direct insight into this issue and also provide a more straight forward means to evaluate the potential bias due to unmodeled finite frequency effects.

5.3 The Laplacian of the amplitude field

For Peer Review

Helmholtz tomography depends heavily on the ability to estimate accurately the gradient of the phase travel time field and the Laplacian of the amplitude field. The Laplacian is generally harder to estimate with a finite station distribution. Although the method to calculate the gradient and Laplacian operators with finite measurements is not unique, the fundamental limitations are similar. Considering the configuration of the USArray with a ~70 km average station spacing, computation of the gradient at each location usually involves at least the nearest 3 to 4 stations (mostly within ~70 km). In constrast, computation of the Laplacian involves 9 to 16 nearby stations (mostly within ~140 km). This restricts the resolution of the Laplacian of amplitude and is reflected in our method that performs minimum curvature surface fitting twice to obtain a smoothly varying Laplacian field. For shorter periods considered here, the Laplacian of amplitude is probably underestimated. Different methods to estimate the Laplacian term, for example by performing a contour integral by utilizing Gauss's law, will suffer from the same limitation. Hence, while the Laplacian of the amplitude term in eq. (2) can be theoretically used to correct for the apparent phase velocity bias, in practice it does not have the same resolving power as measurements based on the travel time gradient alone.

This difference in resolution between the gradient and Laplacian operators will only be important when the phase and amplitude variations are both dominated by small-scale features. Figure 20 summarizes the average correlation coefficient (ρ) and the average correction factor (λ) between the apparent slowness squared bias (α) and the amplitude correction term (β) (discussed in section 3.1) for all earthquakes at each period. At short periods (<50 sec), a smaller overall correlation coefficient ρ (Fig. 20a) is observed, which probably reflects the shorter wavelength interference patterns that are harder to resolve with the Laplacian operator. This is consistent with the overall > 1 average best fitting correction factor λ at short periods (Fig. 20b), which indicates an underestimation of the Laplacian term. Note that the reduction of the correction factor λ at long periods, which eventually becomes lower than the theoretical value of unity, is probably due to the reduced accuracy of amplitude measurements at long periods. When the Laplacian of amplitude has a larger uncertainty, using a smaller correction factor can potentially lead to smaller spatial variations in velocity measurements but can also fall short of correcting the systematic bias.

The presence of dense regional arrays such as the EarthScope Flexible Array can potentially improve the accuracy of the Laplacian operator. This may be important to resolve small-scale anomalies and sharpen the structural boundaries. Whether the spurious 1-psi anisotropy signals can be suppressed with the presence of such arrays also remains an open question.

6. Conclusions

For Peer Review

The fundamental philosophy behind both eikonal and Helmholtz tomography is to directly and locally estimate surface wave phase velocities by interpreting the observed wavefield through an underlying wave equation. In contrast to traditional tomography methods in which a forward operator is needed to construct the inverse operator, no forward modeling is needed and no inversion is performed. Rather, only spatial operators are applied to the observations. Hence, for eikonal and Helmholtz tomography, the accuracy of the method is not controlled by the accuracy of forward calculations. It is controlled mainly by the accuracy of the observed wavefield and the underlying wave equation.

In this study, we show that eikonal tomography based on the eikonal equation (Lin et al. 2009), which accounts naturally for off great circle propagation, can be improved by also accounting for finite frequency effects when accurate amplitude measurements are available. By performing phase front tracking and amplitude measurement, we demonstrate that the Helmholtz tomography method clearly resolves both isotropic and azimuthally anisotropic structures better than the eikonal tomography method, particularly at longer periods (>50 sec).

Although statistics (Fig. 9a, 11c, and13e) suggest that Helmholtz tomography outperforms the eikonal tomography method even at short periods, our results suggest that the differences are small at short periods (<50 sec) where finite frequency effects are less severe. This justifies the use of eikonal tomography for ambient noise applications (Lin et al., 2009; Lin et al., 2011), which often do not extend above 50 sec period. It must be noted, however, that this period criterion is resolution dependent and will be somewhat different for different applications.

The fact that spurious 1-psi azimuthal anisotropy, which should be considered as a clear indicator of systematic bias in anisotropy, remains strong near structural boundaries at long periods (> 50 sec) suggest that Helmholtz tomography, as we effect it here, remains insufficient to model the observations fully. Two separate lines of investigation may lead to a better understanding of this apparent deficiency. First, it would be useful to investigate the accuracy of Helmholtz tomography based on numerical simulations or with regional arrays with a higher station density such as the EarthScope USArray Flexible Array. Second, it would also be useful to investigate whether the Helmholtz equation is only valid for instantaneous frequency measurements. Because the frequency-time analysis that we employ involves resolving both phase and amplitude in a finite frequency band, strictly speaking, they are not instantaneous frequency measurements. The severity of systematic bias in both the isotropic and 2-psi azimuthally anisotropic results at periods above ~50 sec will be understood better if analyses are performed.

For Peer Review

Acknowledgements

Instruments (data) used in this study were made available through EarthScope (www.earthscope.org; EAR-0323309), supported by the National Science Foundation. The facilities of the IRIS Data Management System, and specifically the IRIS Data Management Center, were used for access the waveform and metadata required in this study. The IRIS DMS is funded through the National Science Foundation and specifically the GEO Directorate through the Instrumentation and Facilities Program of the National Science Foundation under Cooperative Agreement EAR-0552316. This work has been supported by NSF grants EAR-0711526 and EAR-0844097.

Figure captions

Figure 1. The USArray Transportable Array (TA) stations used in this study are identified by black triangles. The two stars identify locations used later in the paper. Red lines mark the tectonic boundaries in the western US.

Figure 2. (a) The earthquakes used in this study. Circles mark the location of the earthquakes, the star is the center of our study region, and the lines between circles and the star are great-circle paths. The two green circles and paths mark the earthquakes used in Fig. 3 and 4 and the blue circle and path mark the earthquake used in Fig. 19. (b) Number of events with at least 50 stations with good measurements at each period.

Figure 3. (a)-(b) The 60 sec Rayleigh wave observed phase travel time and amplitude maps for the April 7th, 2009 earthquake near Kuril Islands (Ms=6.8). The stations with available phase travel time and amplitude measurements used to construct the maps are shown as triangles. Contours are separated by intervals of 60 sec in (a) and 100 nm/sec in (b). The arrow in (a) indicates the approximate direction of wave propagation. (c)-(d) Similar to (a)-(b) but for the February 14th, 2007 earthquake near Easter Island (Ms=5.7). Contours in (d) are separated by intervals of 5 nm/sec.

Figure 4. (a) The apparent phase velocity map derived from Figure 3a based on eq. (1). (b) The amplitude correction term in eq. (2) derived from Figure 3b. (c) The corrected phase velocity map derived from (a) and (b) based on eq. (2). Same as (a)-(c) but for results derived from Figure 3c-d.

Figure 5. (a) The normalized histogram for the 60 sec Rayleigh wave apparent phase velocity measurements at a point in southern Washington (star in Fig. 1) based on all available earthquakes. (b) Same as (a) but for a point in western New Mexico (star in Fig. 1). (c)-(d) Same as (a)-(b) but for the corrected phase velocity measurements. The mean and standard deviation of the mean, which are used to estimate the final isotropic phase velocity and its uncertainty, at each location is shown.

Figure 6. (a) The 60 sec Rayleigh wave apparent isotropic phase velocity map in the western US based on Eikonal tomography. (b) Same as (a) but for the corrected phase velocity map based on

For Peer Review

Helmholtz tomography. (c) The difference between (b) and (a). CL: Clear Lake Volcanic Field; IA: Isabella Anomaly; LV: Long Valley Caldera; NB: Newberry Caldera; SY: Snake River Plain/Yellowstone hot spot track; CP: Colorado Plateau.

Figure 7. (a) The uncertainty for the 60 sec Rayleigh wave apparent isotropic phase velocity map. (b) Same as (a) but for the corrected isotropic phase velocity map.

Figure 8. (a)-(c) Same as Figure 6 but for the 40 sec Rayleigh wave. (d)-(f) Same as (a)-(c) but for the 80 sec Rayleigh wave.

Figure 9. (a) Average uncertainties for the apparent and corrected isotropic phase velocity maps at each period. (b) The standard deviation of the differences between the apparent and corrected isotropic phase velocity maps at each period.

Figure 10. (a) The 60 sec Rayleigh wave directionally dependent apparent phase velocity measurements at a point in southern Washington (star in Fig. 1). Each error bar presents the mean and the standard deviation of the mean of all measurements within each 20° bin. The solid green line is the best fitting curve of 1-psi plus 2-psi azimuthal anisotropy based on eq. (3). (b) Same as (a) but for a point in western New Mexico (star in Fig. 1). (c)-(d) Same as (a)-(b) but for the corrected phase velocity measurements.

Figure 11. (a) The best fitting chi-squared value for the directionally dependent apparent phase velocity measurements using eq. (3). (b) Same as (a) but for the corrected phase velocity measurements. (c) The spatial averaged best fitting chi-squared value for apparent and corrected measurements at each period.

Figure 12. (a) The amplitude of the 60 sec Rayleigh wave apparent 1-psi anisotropy based on eikonal tomography. The 1-psi fast directions at locations with 1-psi amplitude larger than 2% are presented with arrows where arrows point in the fast propagation directions. (b) Same as (a) but for the 1-psi anisotropy based on Helmholtz tomography. (c)-(d) normalized histogram of 1-psi anisotropy amplitudes shown in (a) and (b), respectively.

Figure 13. (a)-(b) Same as Figure 12a-b but for the 40 sec Rayleigh wave. (c)-(d) Same as (a)-(b) but for the 80 sec Rayleigh wave. (e) The spatially averaged 1-psi amplitude for apparent and corrected measurement at each period.

Figure 14. (a) The apparent 2-psi anisotropy for the 60 sec Rayleigh wave based on eikonal tomography where the amplitude and fast direction are summarized by the orientation and the length of the red bars. The amplitude of 2-psi anisotropy is also shown by the background color. (b) Same as (a) but with the corrected 2-psi anisotropy based on Helmholtz tomography. (c) The normalized histogram of fast direction differences between (a) and (b) where only locations with 2-psi anisotropy amplitudes both larger than 0.5% are compared.

For Peer Review

Figure 15. (a)-(c) Same as Figure 14a-c but for 40 sec Rayleigh wave. (d)-(f) Same as (a)-(c) but for the 80 sec Rayleigh wave.

Figure 16. (a)The standard deviation of 2-psi fast direction differences between apparent and corrected measurements across the western US at each period. Only locations with 2-psi anisotropy amplitudes larger than 0.5% are compared. (b) The vector correlation coefficients for the 2-psi fast directions observed between 40 sec and other periods based on either eikonal (red) or Helmholtz (green) tomography. Only locations with observed 2-psi anisotropy amplitude larger than 0.5 are used in the calculation.

Figure 17. (a) The apparent slowness squared bias α derived from Figure 3d and Figure 6b. (b) Same as Figure 4e. (c) The relation between the apparent bias and the amplitude correction term based on (a) and (b) where each point represents the results at a grid point on the maps. The green dashed line is the best fitting straight line based on eq. (4) The value of the slope (correction factor λ) and the correlation coefficient (ρ) are also shown.

Figure 18. (a)-(b) The normalized histograms of the correlation coefficient (ρ) and correction factor (λ) for all events for 60 sec Rayleigh wave. (c) The relationship between the correlation coefficient and the correction factor over all earthquakes. The solid green line represents the theoretical value of the correction factor based on eq. (2). (d) The relationship between the correlation coefficient ρ and the average of the measured amplitudes for each event.

Figure 19. (a)-(b) The 60 sec Rayleigh wave phase and amplitude maps for the September 28th, 2007 earthquake near Loyalty Islands (Ms=6.6; blue circle in Fig. 2a). Contours in (a) and (b) are separated by intervals of 60 sec and 5 nm/sec, respectively. (c)-(d) Same as Figure 4a-b but with results derived from (a) and (b). (e) Same as Figure 17c but for the Loyalty Island event. (f) Same as Figure 4c but derived from (c) and (d).

Figure 20. (a) The average correlation coefficient (ρ) between the apparent slowness squared bias (α) and the amplitude correction term (β) for all events as a function of period. (b) The average correction factor (λ) for all events as a function of period

For Peer Review

References

Barmin, M.P., Ritzwoller, M.H. & Levshin, A.L., 2001. A fast and reli- able method for surface wave tomography. *Pure appl. Geophys.,* **158**(8), 1351–1375.

Bensen, G.D., Ritzwoller, M.H., Barmin, M.P., Levshin, A.L., Lin, F., Moschetti, M.P., Shapiro, N.M. & Yang, Y., 2007. Processing seismic ambient noise data to obtain reliable broad-band surface wave dispersion measurements. *Geophys. J. Int.,* **169**(3), 1239–1260.

Bodin, T. & Maupin, V., 2008. Resolution potential of surface wave phase velocity measurements at small arrays. *Geophys. J. Int.*, **172**: 698–706. doi: 10.1111/j.1365-246X.2007.03668.x

Dalton, C.A. & Ekstrom, G., 2006. Constraints on global maps of phase velocity from surface-wave amplitudes, *Geophys. J. Int*., **167**, 820–826.

Ekstrom, G., Tromp, J. & Larson, E.W.F., 1997. Measurements and global models of surface wave propagation, *J. geophys. Res*, **102**, 8137–8157.

Friederich, W., Hunzinger, S. & Wielandt, E., 2000. A note on the interpreta- tion of seismic surface waves over three-dimensional structures, *Geophys. J. Int.,* **143**, 335–339.

Levshin, A.L. & Ritzwoller, M.H., 2001. Automated detection, extraction, and measurement of regional surface waves. *Pure appl. Geophys*., **158**(8), 1531–1545.

Liang, C., & Langston, C. A., 2009. Wave gradiometry for USArray: Rayleigh waves, *J. Geophys. Res.*, **114**, B02308, doi:10.1029/2008JB005918.

Lin, F., M.H. Ritzwoller, J. Townend, M. Savage, S. Bannister, 2007. Ambient noise Rayleigh wave tomography of New Zealand, *Geophys. J. Int.,* **173**, 281–198.

Lin, F., Moschetti, M.P. & Ritzwoller, M. H., 2008. Surface wave tomography of the western United States from ambient seismic noise: Rayleigh and Love wave phase velocity maps. *Geophys. J. Int.*, **173**(1), 281–298.

Lin, F., Ritzwoller, M.H. & Snieder, R., 2009. Eikonal tomography: surface wave tomography by phase front tracking across a regional broad-band seismic array. *Geophys. J. Int.*, **177**(3), 1091–1110.

Lin, F.-C. & Ritzwoller, M. H., 2010. Empirically determined finite frequency sensitivity kernels for surface waves. *Geophys. J. Int.*, **182**: 923–932. doi: 10.1111/j.1365-246X.2010.04643.x

Lin, F.C. and M.H. Ritzwoller, 2011. Apparent anisotropy in inhomogeneous isotropic media, *Geophys. J. Int.*, submitted.

Lin, F.C., M.H. Ritzwoller, Y. Yang, M.P.Moschetti, and M.J. Fouch, 2011. Complex and variable crustal and uppermost mantle seismic anisotropy in the western United States. *Nature Geoscience,* **4**, 55–61.

Pollitz, F.F. , 2008. Observations and interpretation of fundamental mode Rayleigh wavefields recorded by the Transportable Array (USArray), *Geophys. J. Int.,* **173**, 189-204.

For Peer Review

Pollitz, F. F. & Snoke, J. A., 2010, Rayleigh-wave phase-velocity maps and three-dimensional shear velocity structure of the western US from local non-plane surface wave tomography. *Geophys. J. Int.*, **180**, 1153–1169.

Ritzwoller, M.H., F.C. Lin, and W. Shen, 2011. Ambient noise tomography with a large seismic array, *Compte Rendus Geoscience*, in press.

Schmandt, B. & Humphreys, E., 2010, Complex subduction and small-scale convection revealed by body-wave tomography of the western United States upper mantle, *Earth planet. Sci. Lett.*, **297**, 435–445.

Smith, M.L. & Dahlen, F.A., 1973. Azimuthal dependence of Love and Rayleigh-wave propagation in a slightly anisotropic medium, *J. geophys. Res.,* **78**, 3321–3333.

Smith, W.H.F. & Wessel, P., 1990. Gridding with continuous curvature splines in tension, *Geophysics*, **55**, 293–305.

Tape, C., Liu, Q., Maggi, A. & Tromp, J., 2010. Seismic tomography of the southern California crust based on spectral-element and adjoint methods, *Geophys. J. Int.*, **180**, 433–462.

Trampert, J. & Woodhouse, J.H., 1996. High resolution global phase velocity distributions, *Geophys. Res. Lett.,* **23**, 21–24.

Tromp, J., Tape, C. & Liu, Q., 2005. Seismic tomography, adjoint methods, time reversal and banana-doughnut kernels. *Geophys. J. Int.*, **160**,195–216. doi: 10.1111/j.1365-246X.2004.02453.x

Wielandt, E., 1993. Propagation and structural interpretation of non-plane waves, *Geophys. J. Int.*, **113**, 45–53.

Yang, Y. & Forsyth, D., 2006. Regional tomographic inversion of the amplitude and phase of Rayleigh waves with 2-D sensitivity kernels, *Geophys. J. Int.*, **166**, 1148–1160.

Yang, Y., Ritzwoller, M.H., Lin, F.C., Moschetti, M.P. & Shapiro, N.M., 2008. Structure of the crust and uppermost mantle beneath the western United States revealed by ambient noise and earthquake tomography, *J. geophys. Res.*, **113**, B12310, doi:10.1029/2008JB005833.

Zhou, Y., Dahlen, F.A. & Nolet, G., 2004. Three-dimensional sensitivity kernels for surface wave observables. *Geophys. J. Int.*, **158**, 142–168.

For Peer Review

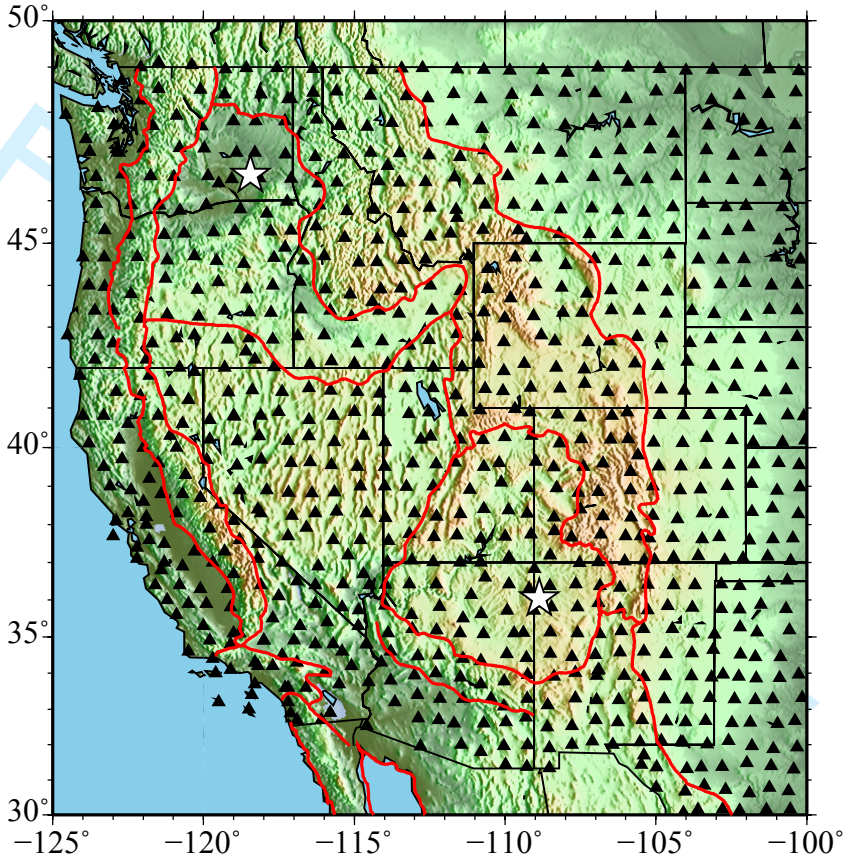

Figure 1

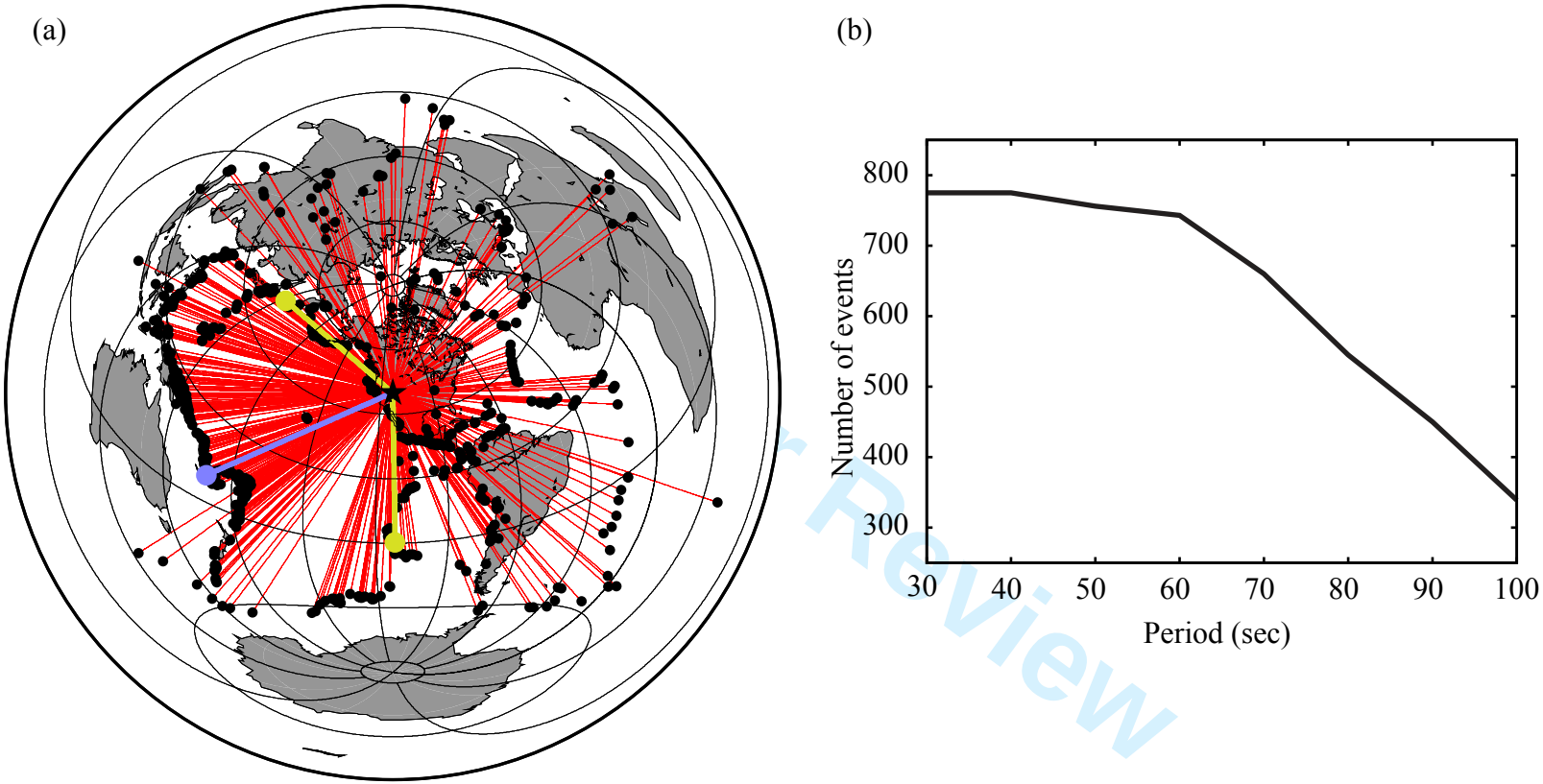

Figure 2

For Review

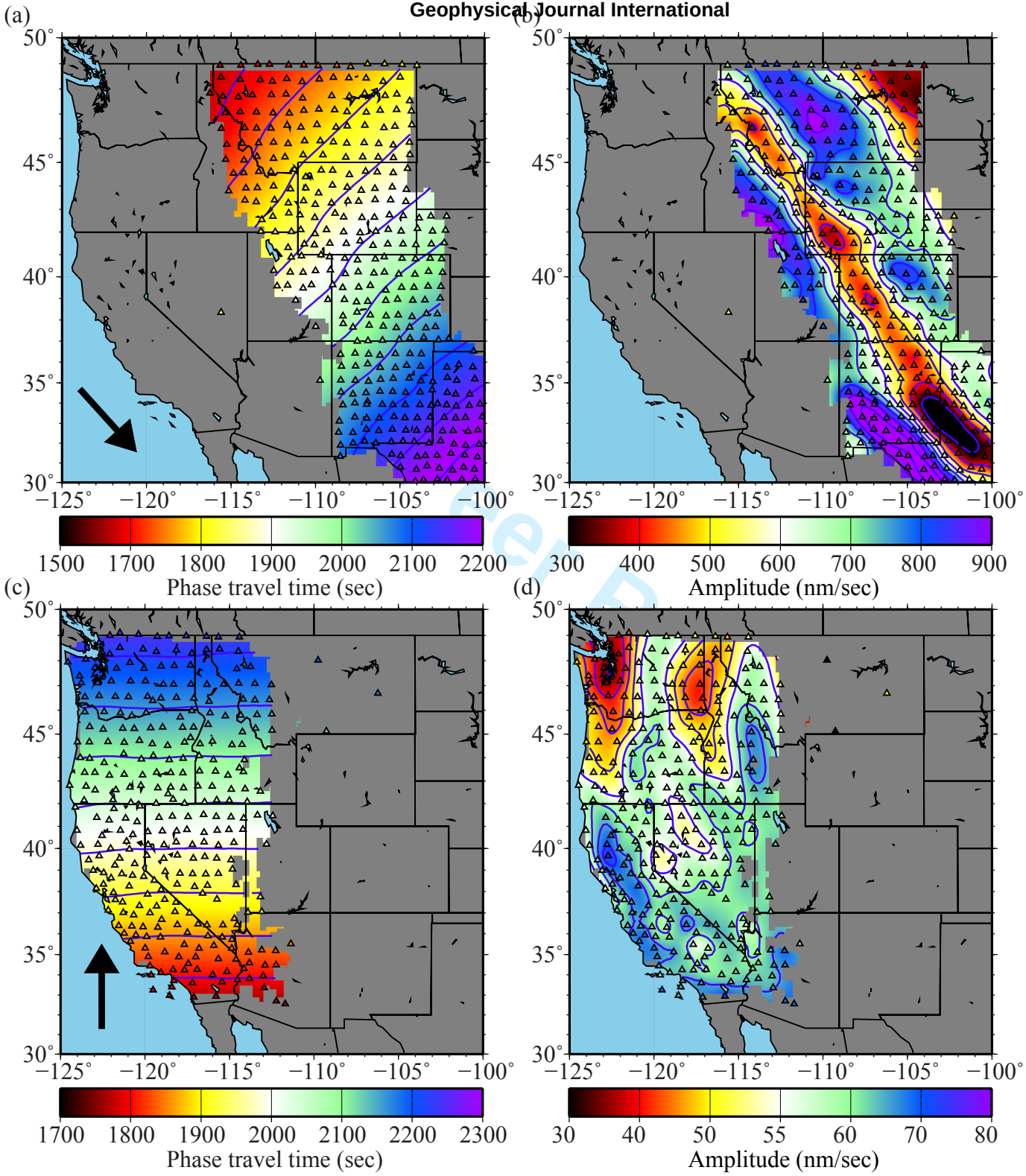
(a)
(b)
(c)
(d)
50°
45°
40°
35°
30°
−125°
−120°
−115°
−110°
−105°
−100°
1500 1700 1800 1900 2000 2100 2200
Phase travel time (sec)
300 400 500 600 700 800 900
Amplitude (nm/sec)
1700 1800 1900 2000 2100 2200 2300
Phase travel time (sec)
30 40 50 55 60 70 80
Amplitude (nm/sec)

Figure 3

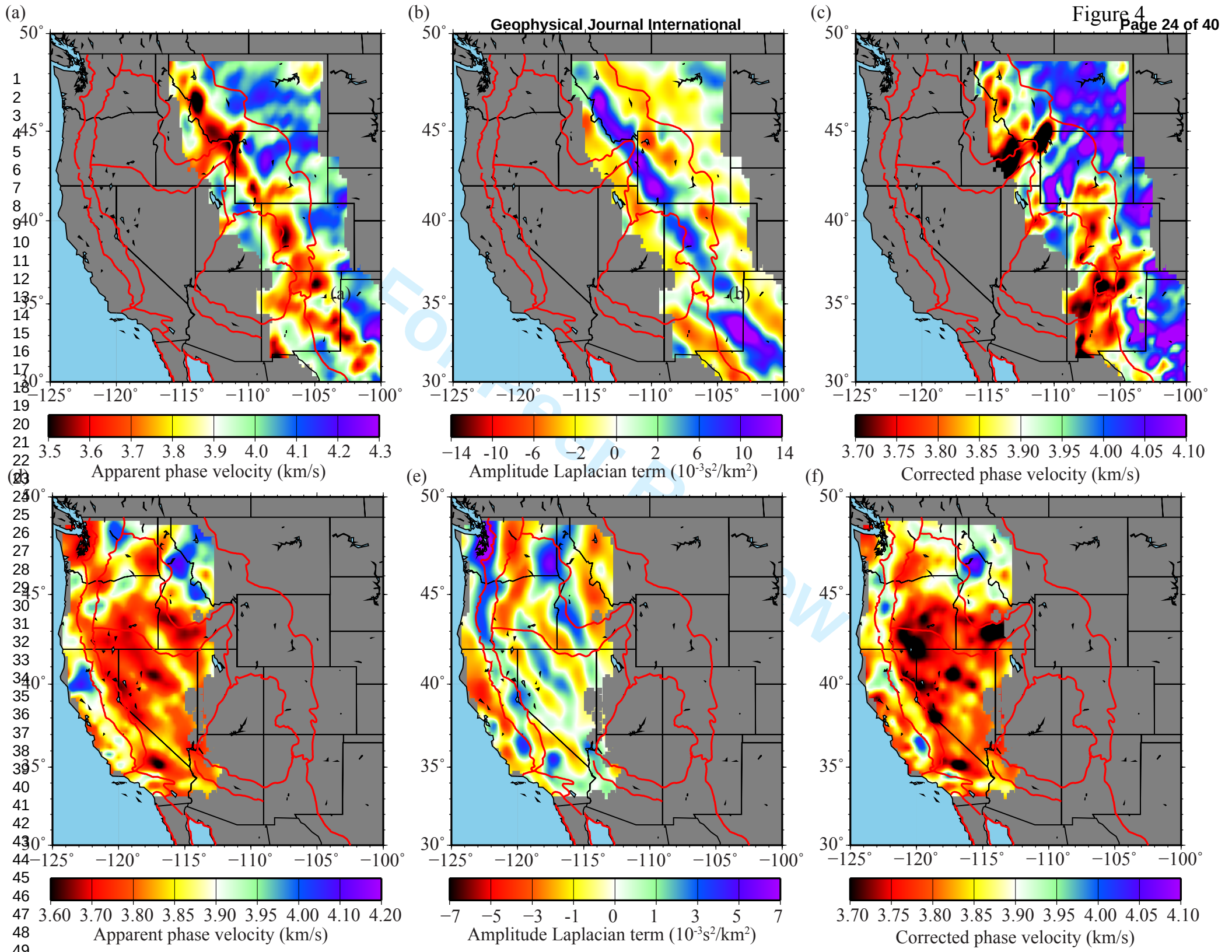
(a)
(b)
(c)
(d)
(e)
(f)
50°
45°
40°
35°
30°
−125°
−120°
−115°
−110°
−105°
−100°
3.5 3.6 3.7 3.8 3.9 4.0 4.1 4.2 4.3
Apparent phase velocity (km/s)
−14 -10 -6 −2 0 2 6 10 14
Amplitude Laplacian term (10-3s2/km2)
3.70 3.75 3.80 3.85 3.90 3.95 4.00 4.05 4.10
Corrected phase velocity (km/s)
3.60 3.70 3.80 3.85 3.90 3.95 4.00 4.10 4.20
Apparent phase velocity (km/s)
−7 −5 −3 -1 0 1 3 5 7
Amplitude Laplacian term (10-3s2/km2)
3.70 3.75 3.80 3.85 3.90 3.95 4.00 4.05 4.10
Corrected phase velocity (km/s)

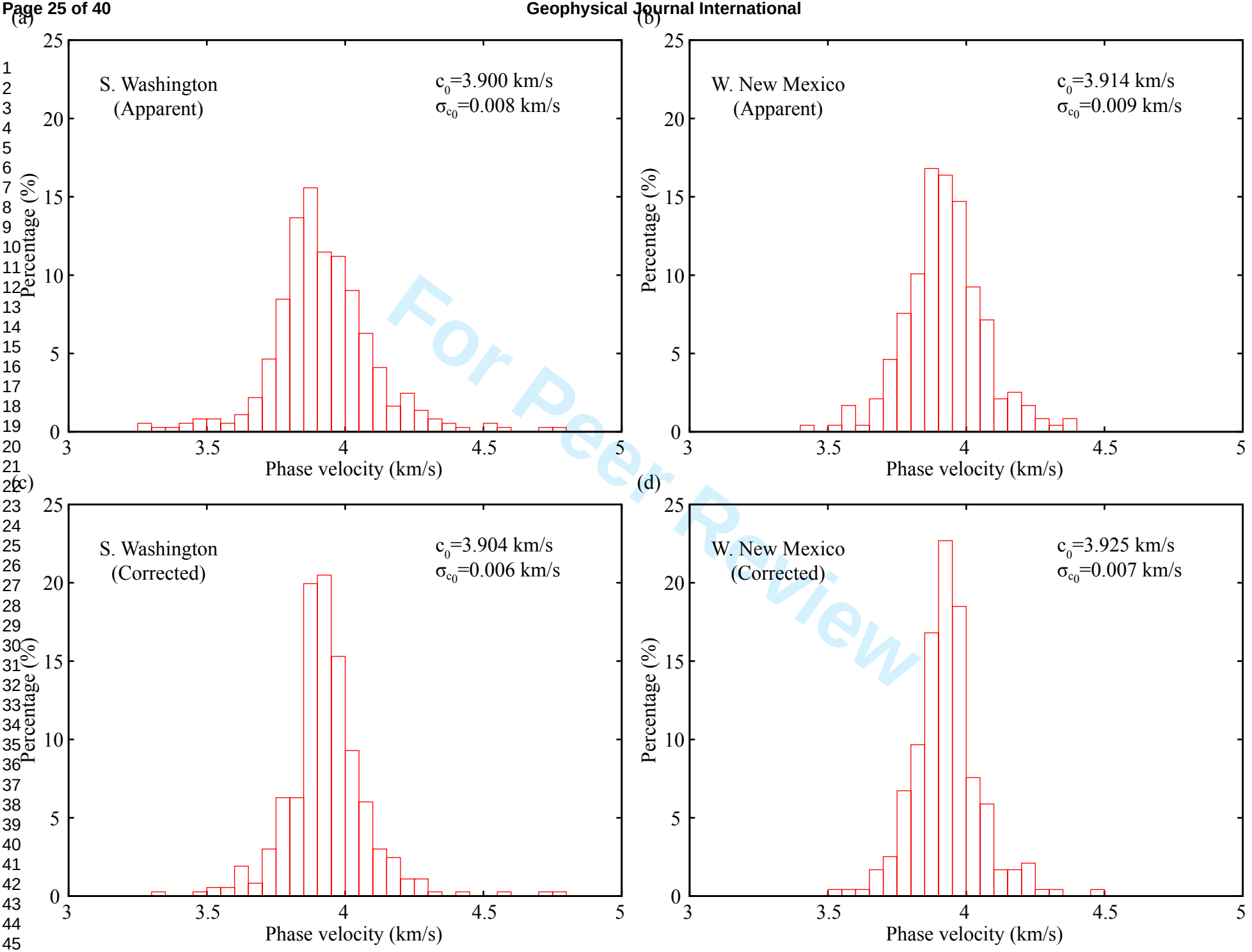

For Peer Review

Figure 5

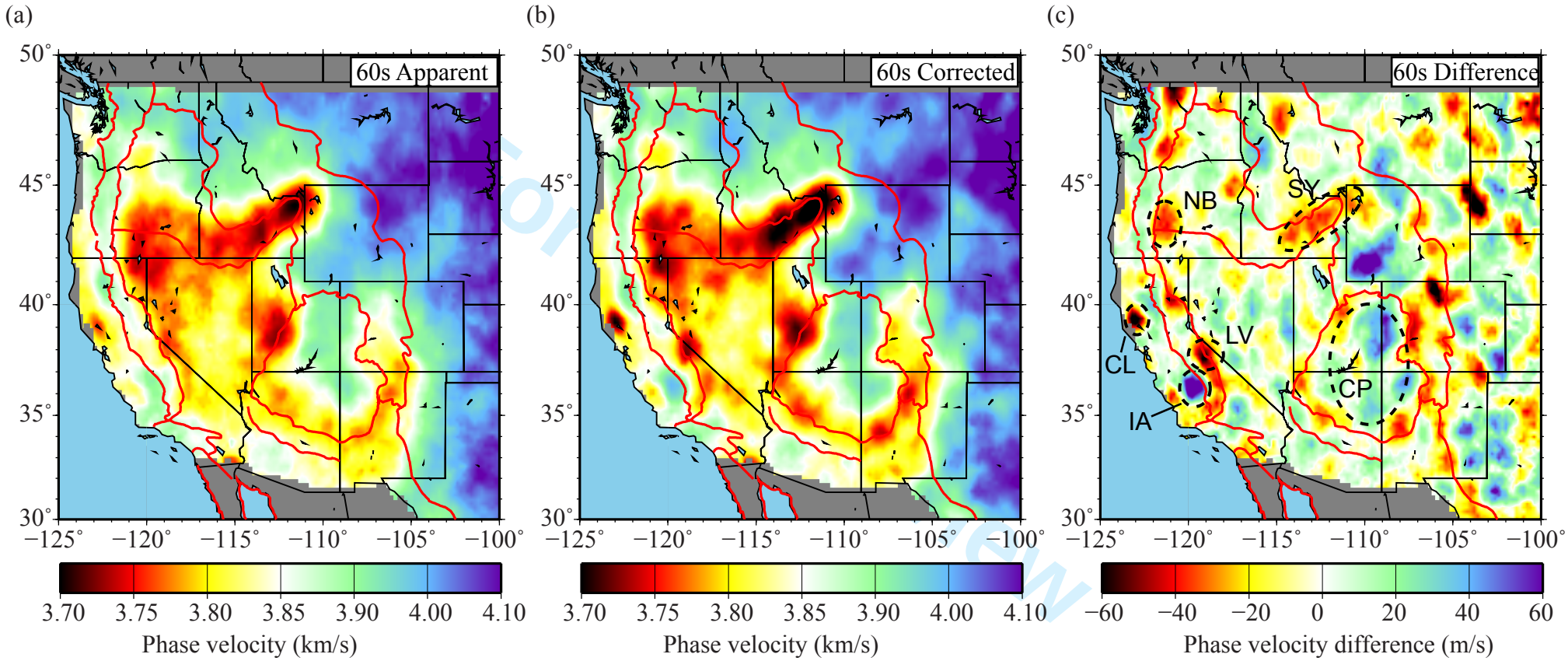
(a)
60s Apparent
(b)
60s Corrected
(c)
60s Difference
NB
SY
LV
CL
CP
IA
50°
45°
40°
35°
30°
−125°
−120°
−115°
−110°
−105°
−100°
3.70
3.75
3.80
3.85
3.90
4.00
4.10
Phase velocity (km/s)
−60
−40
−20
0
20
40
60
Phase velocity difference (m/s)

Figure 6

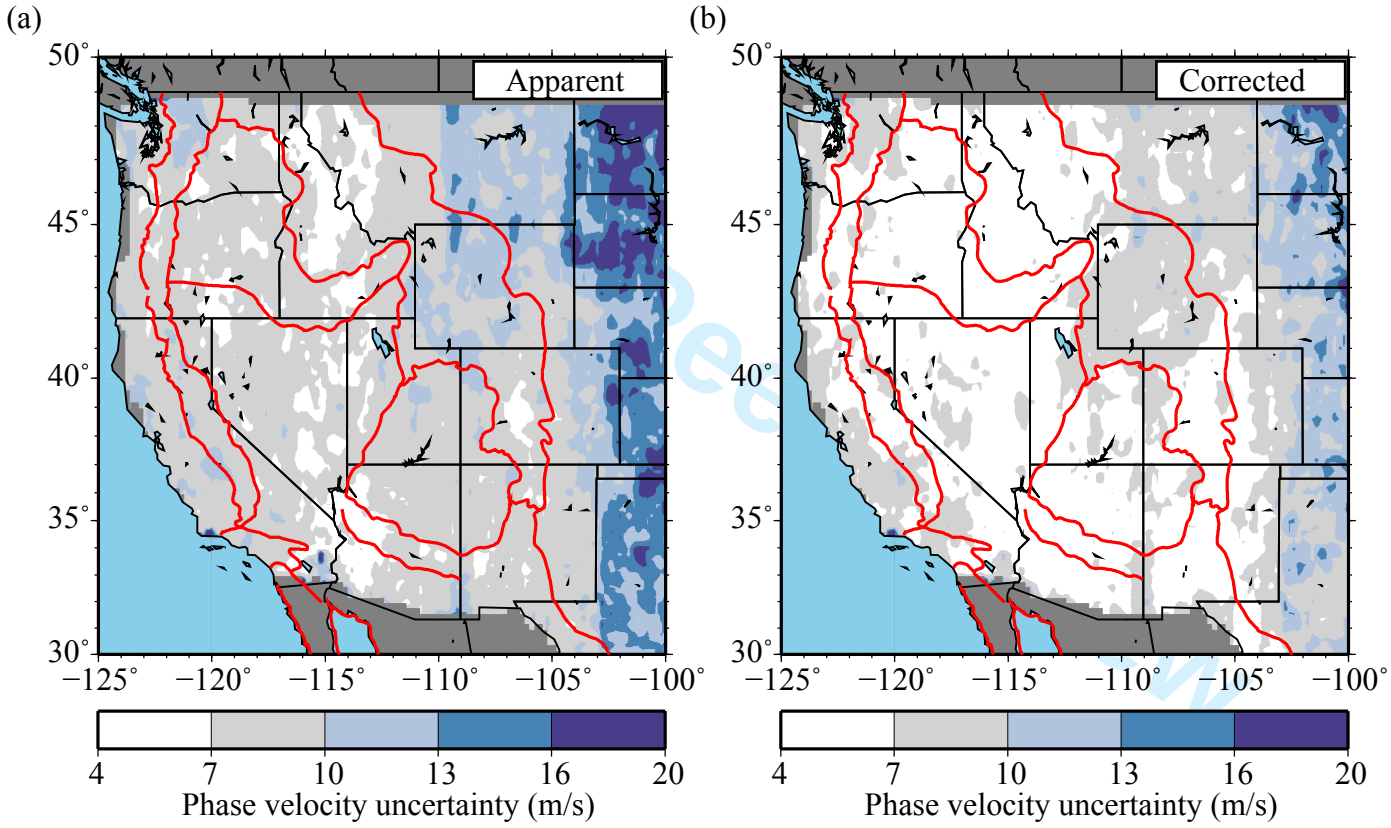
(a)
Apparent
(b)
Corrected
50°
45°
40°
35°
30°
−125°
−120°
−115°
−110°
−105°
−100°
4
7
10
13
16
20
Phase velocity uncertainty (m/s)

Figure 7

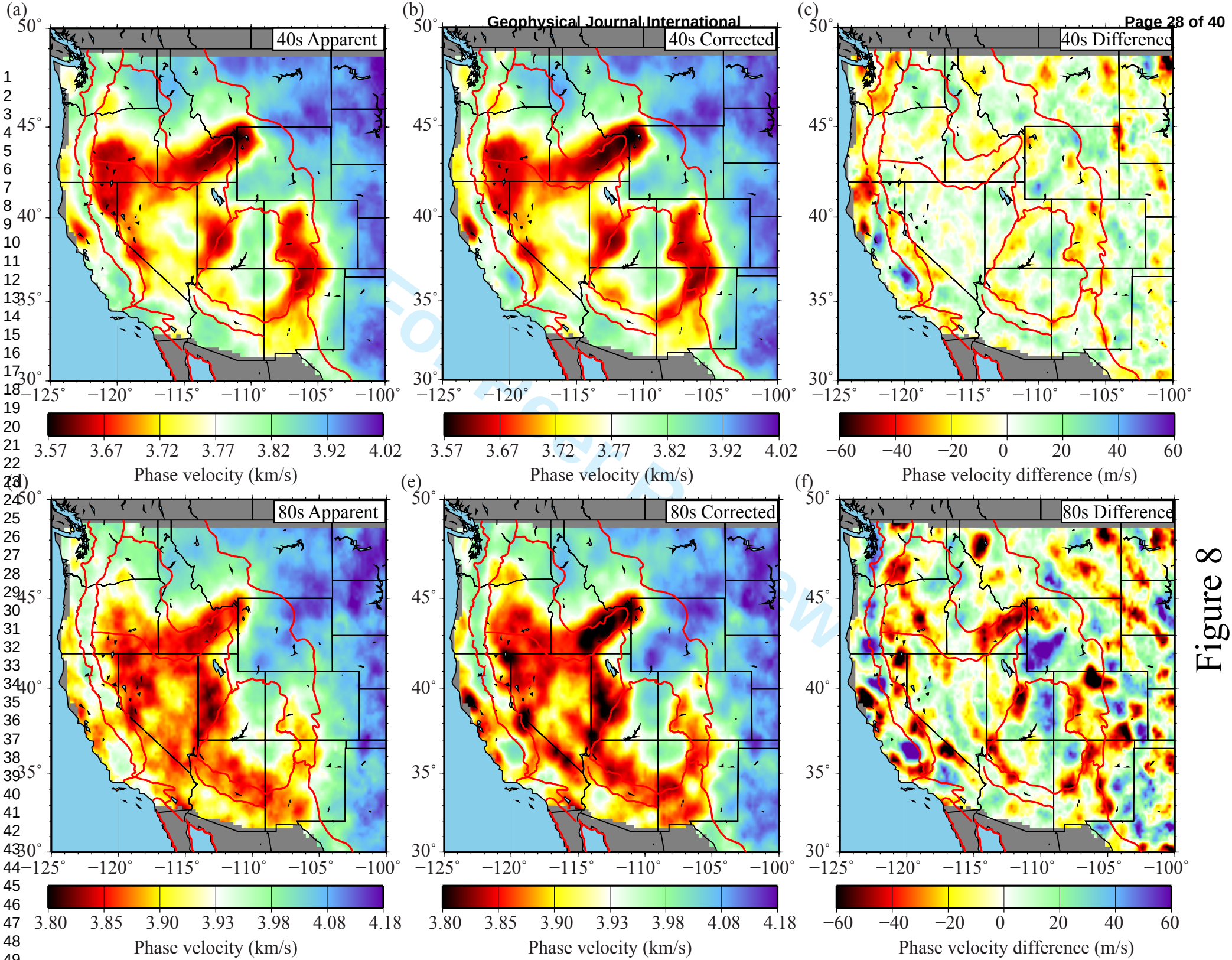

Figure 8

For Peer Review

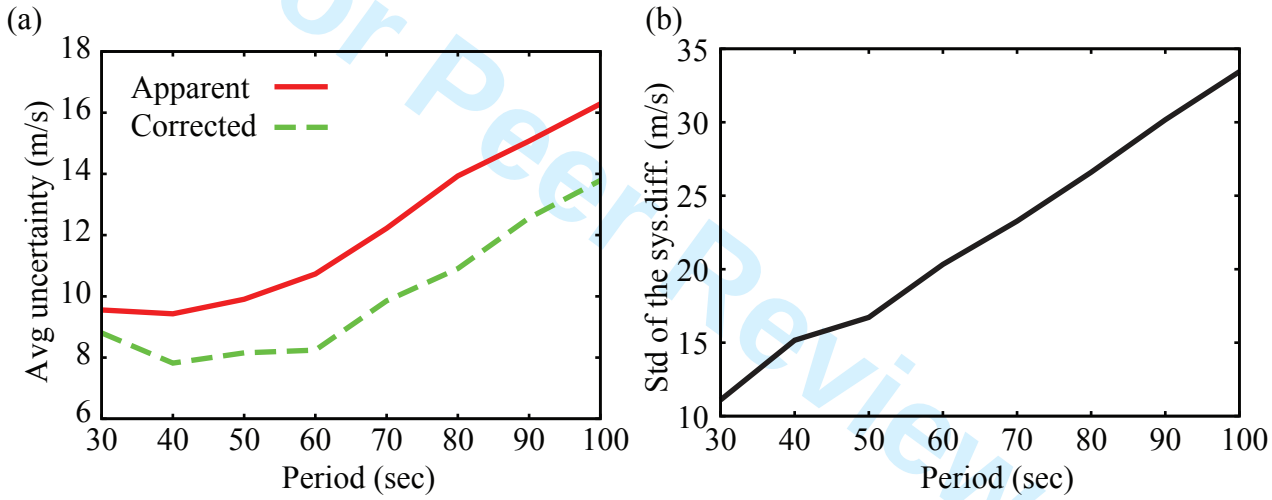

For Peer Review

Figure 9

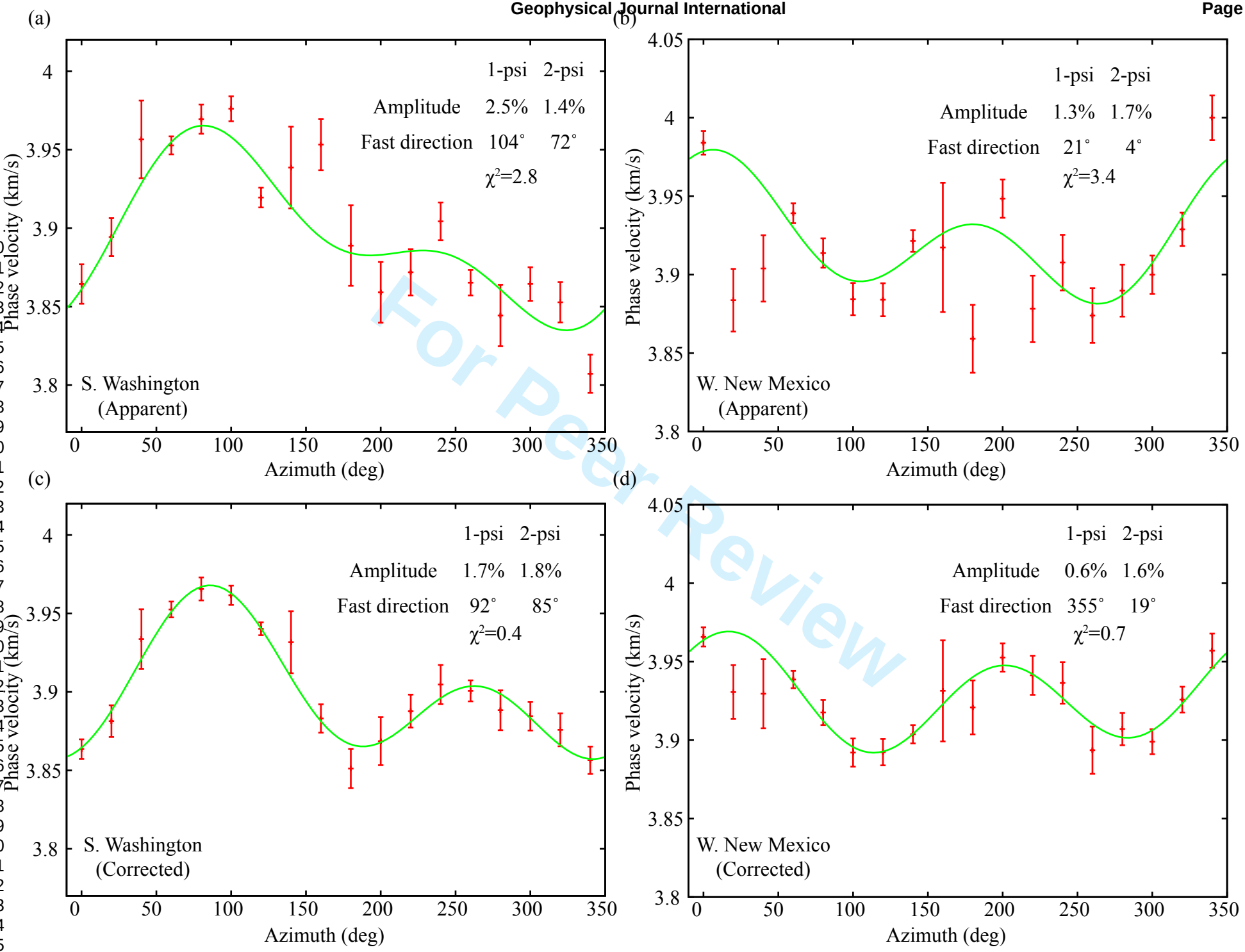

For Peer Review

Figure 10

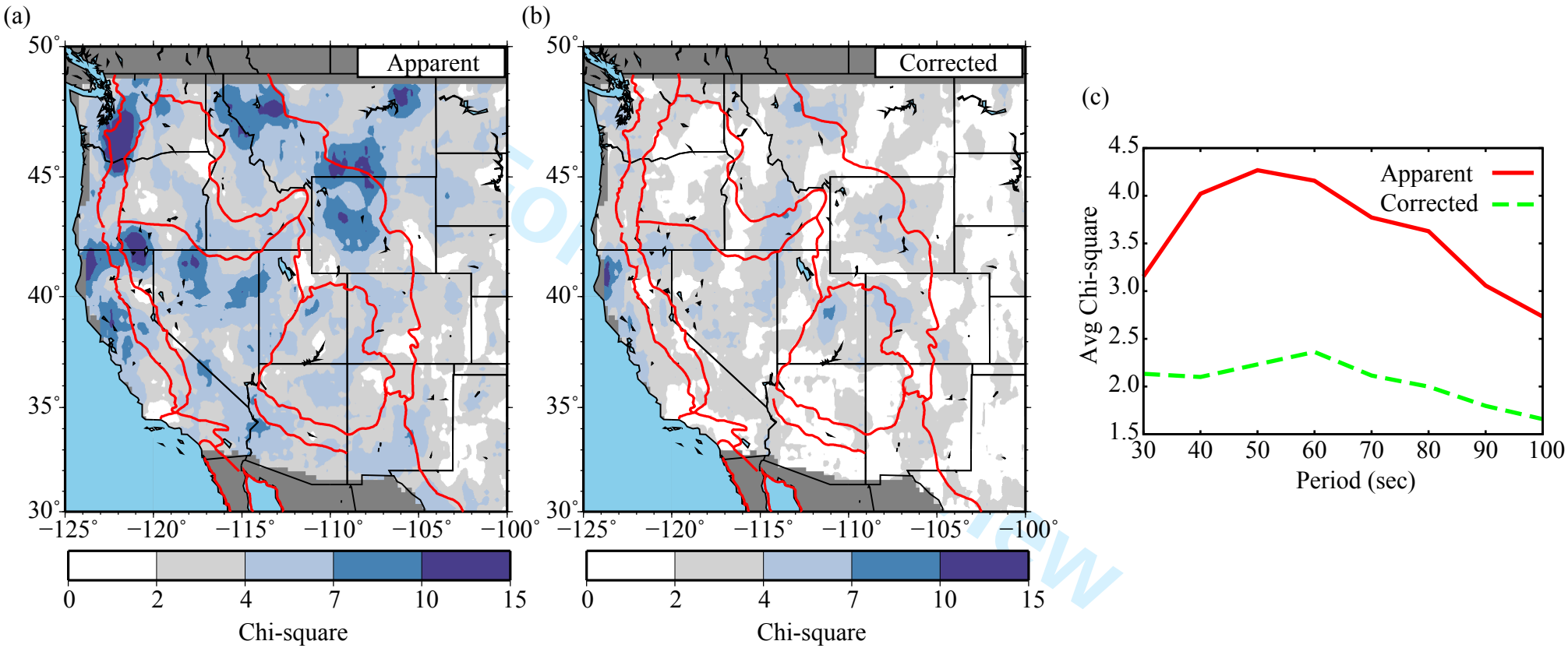
(a)
Apparent
50°
45°
40°
35°
30°
−125°
−120°
−115°
−110°
−105°
−100°
0
2
4
7
10
15
Chi-square
(b)
Corrected
50°
45°
40°
35°
30°
−125°
−120°
−115°
−110°
−105°
−100°
0
2
4
7
10
15
Chi-square
(c)
Apparent
Corrected
Avg Chi-square
4.5
4.0
3.5
3.0
2.5
2.0
1.5
30
40
50
60
70
80
90
100
Period (sec)

Figure 11

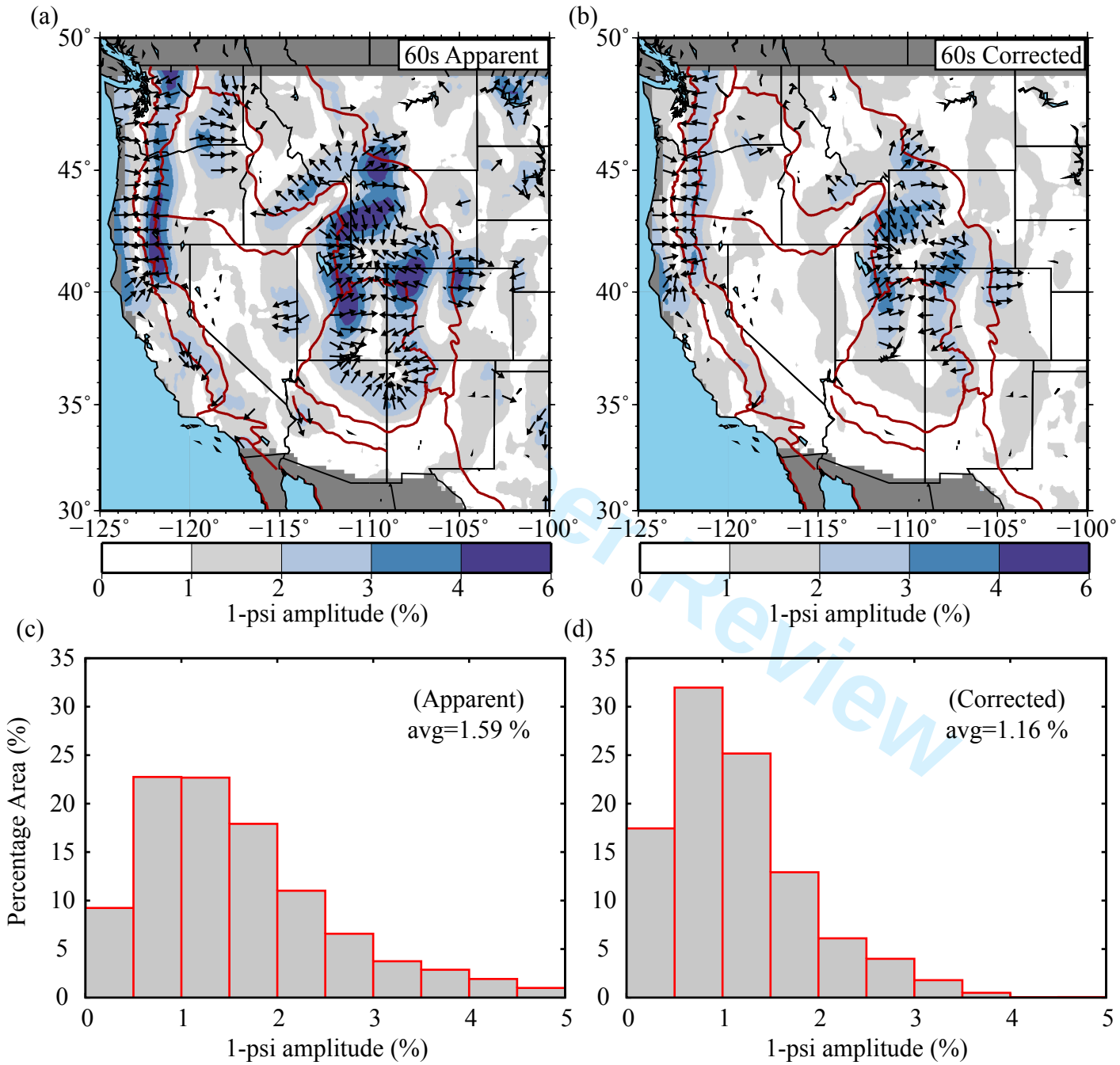

For Peer Review

Figure 12

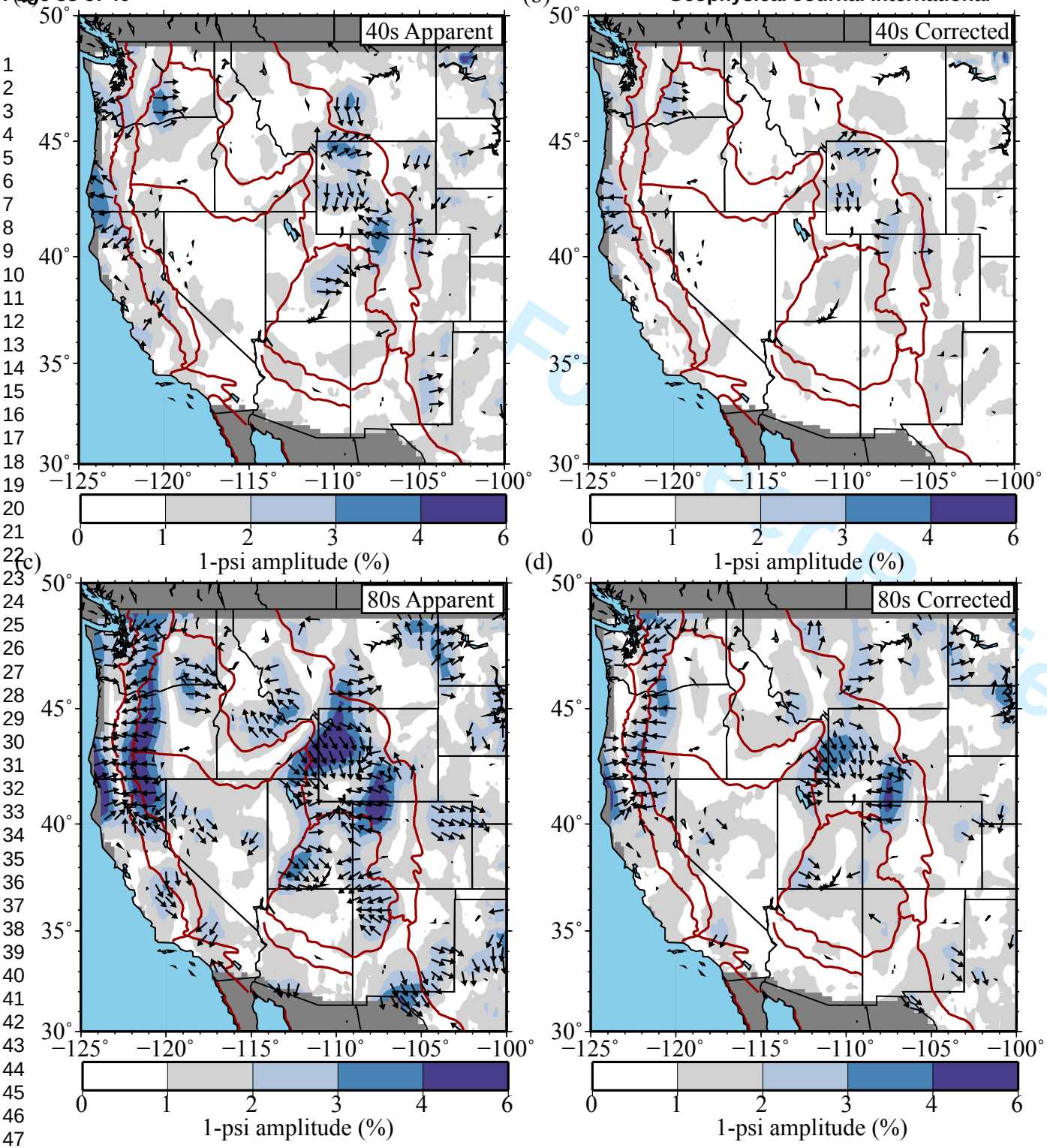
(a)
40s Apparent
(b)
40s Corrected
(c)
80s Apparent
(d)
80s Corrected
50°
45°
40°
35°
30°
−125°
−120°
−115°
−110°
−105°
−100°
0
1
2
3
4
6
1-psi amplitude (%)

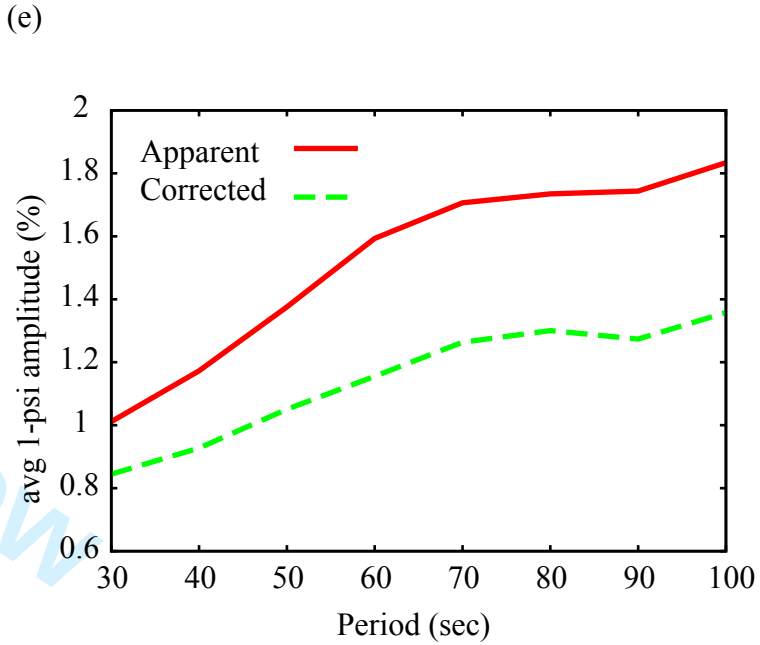
(e)
Apparent
Corrected
avg 1-psi amplitude (%)
Period (sec)
0.6
0.8
1
1.2
1.4
1.6
1.8
2
30
40
50
60
70
80
90
100

Figure 13

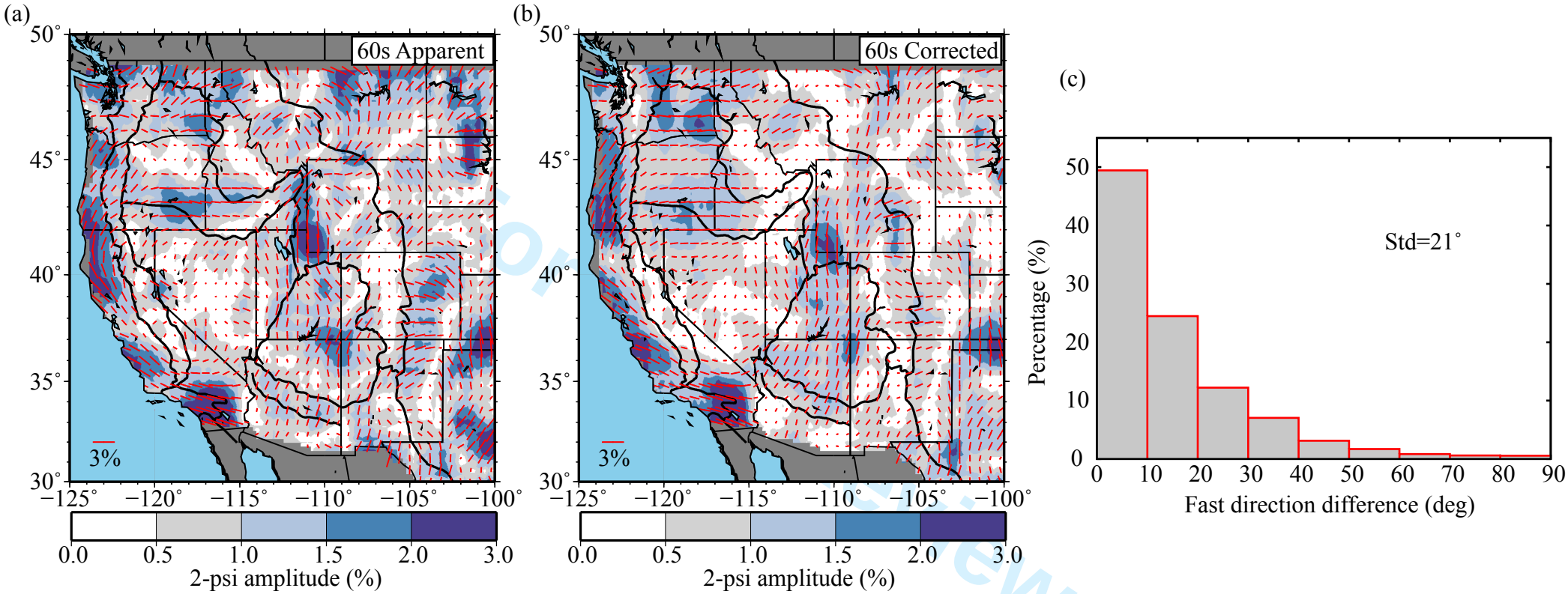
(a)
60s Apparent
3%
50°
45°
40°
35°
30°
−125°
−120°
−115°
−110°
−105°
−100°
0.0
0.5
1.0
1.5
2.0
3.0
2-psi amplitude (%)
(b)
60s Corrected
3%
2-psi amplitude (%)
(c)
Std=21°
Percentage (%)
Fast direction difference (deg)

Figure 14

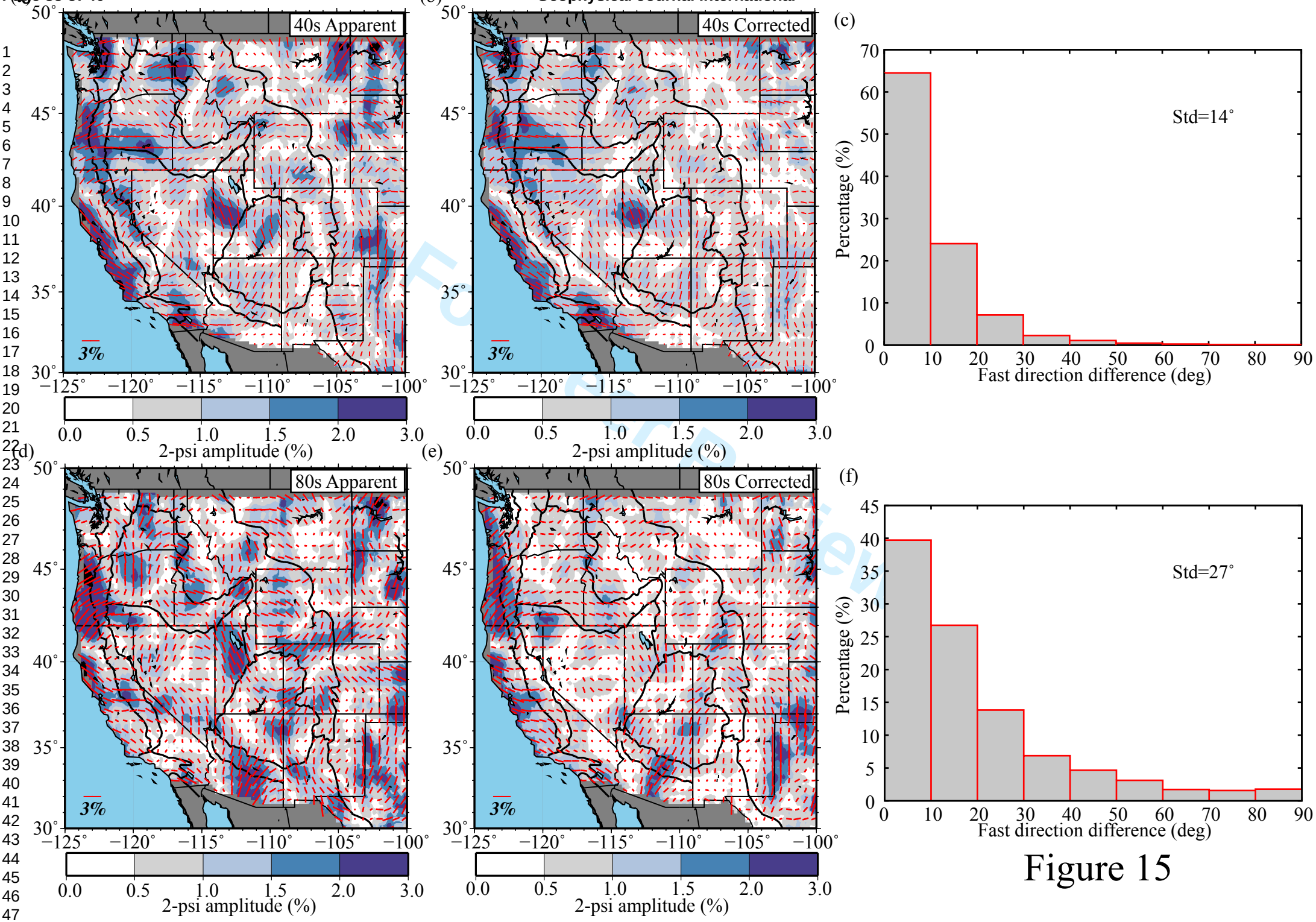
(a)
40s Apparent
(b)
40s Corrected
(c)
Std=14°
Percentage (%)
Fast direction difference (deg)
(d)
80s Apparent
(e)
80s Corrected
(f)
Std=27°
3%
2-psi amplitude (%)

Figure 15

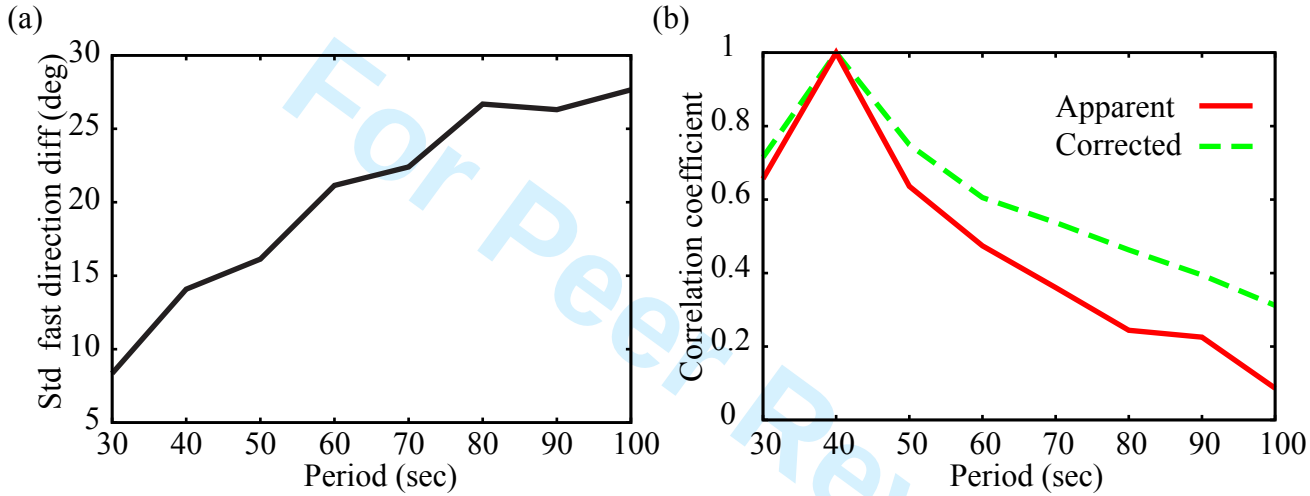

For Peer Review

Figure 16

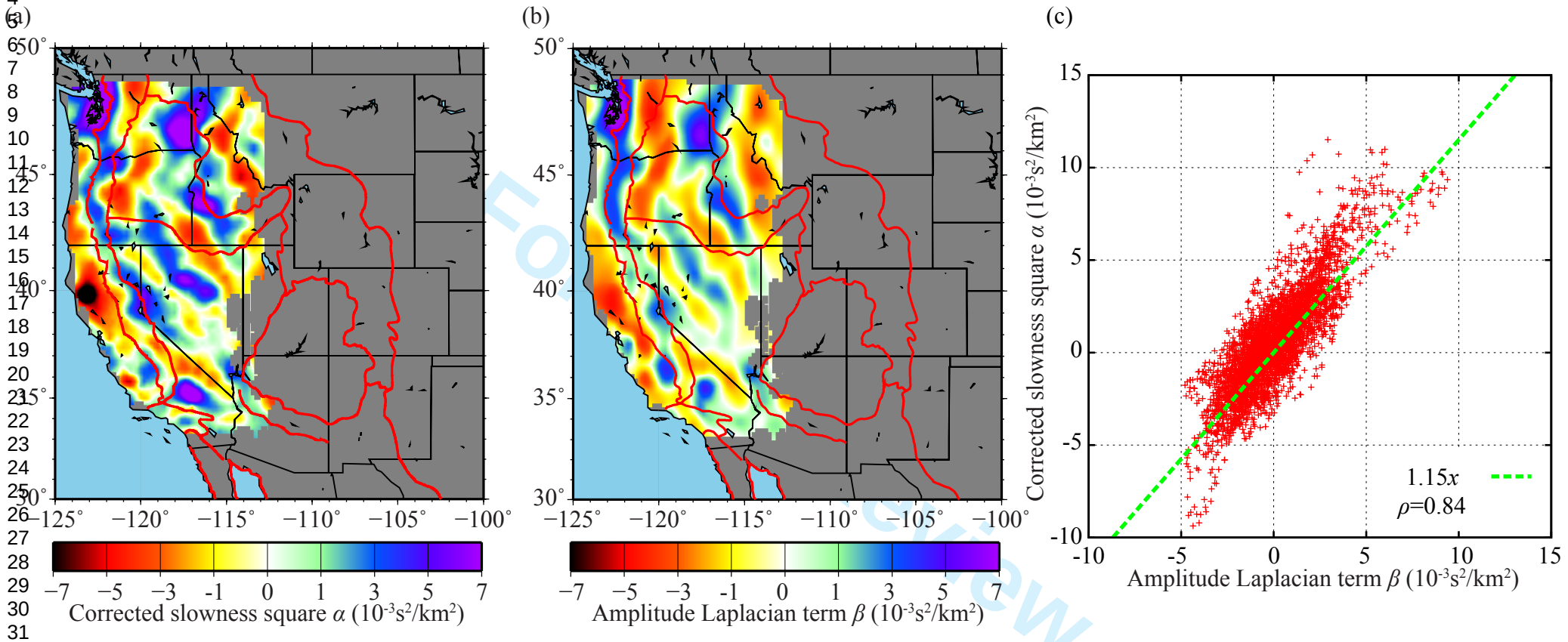
(a)
(b)
(c)
50°
45°
40°
35°
30°
−125°
−120°
−115°
−110°
−105°
−100°
−7 −5 −3 -1 0 1 3 5 7
Corrected slowness square α (10-3s2/km2)
Amplitude Laplacian term β (10-3s2/km2)
Corrected slowness square α (10-3s2/km2)
Amplitude Laplacian term β (10-3s2/km2)
15
10
5
0
-5
-10
1.15x
ρ=0.84

Figure 17

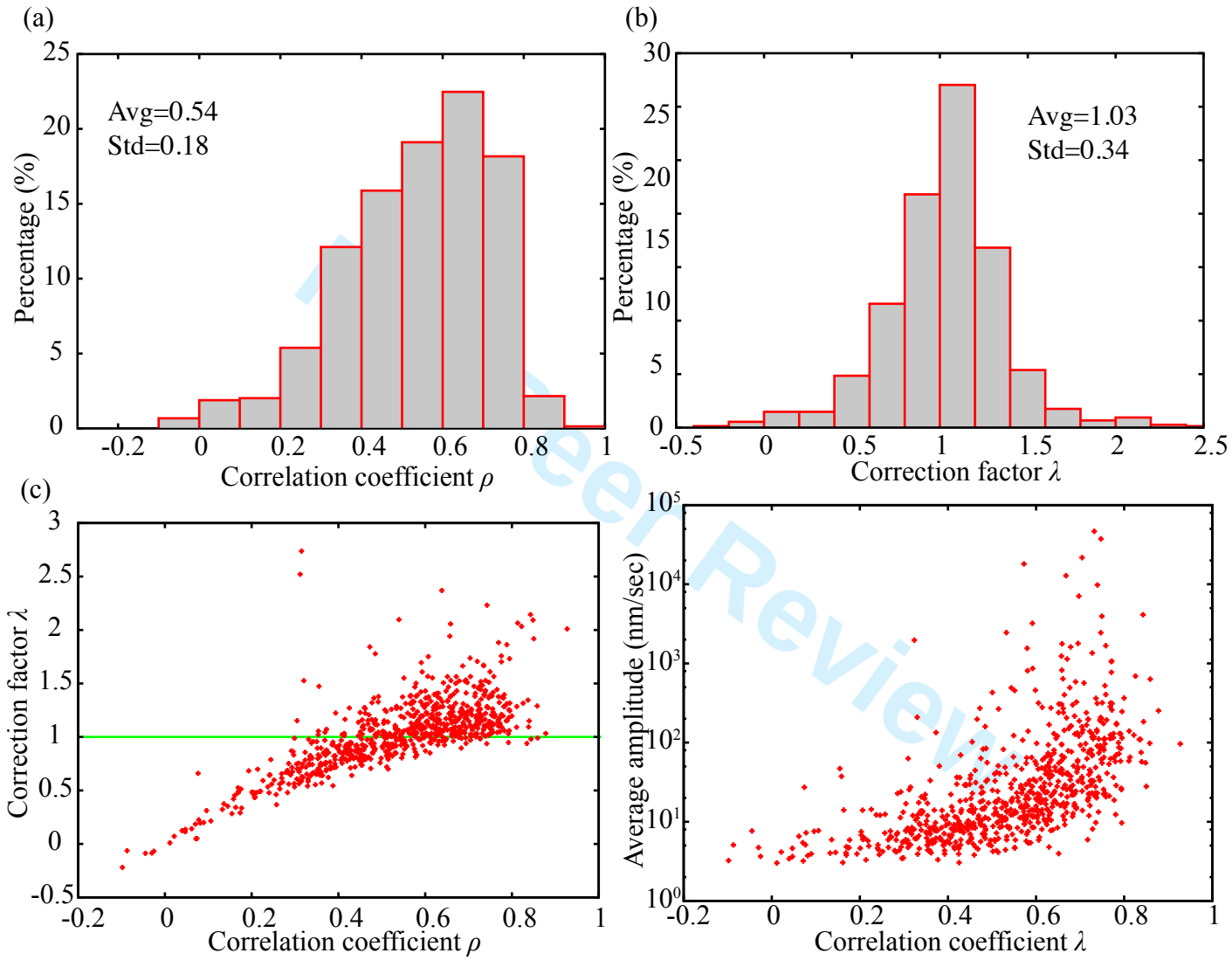

Figure 18

For Peer Review

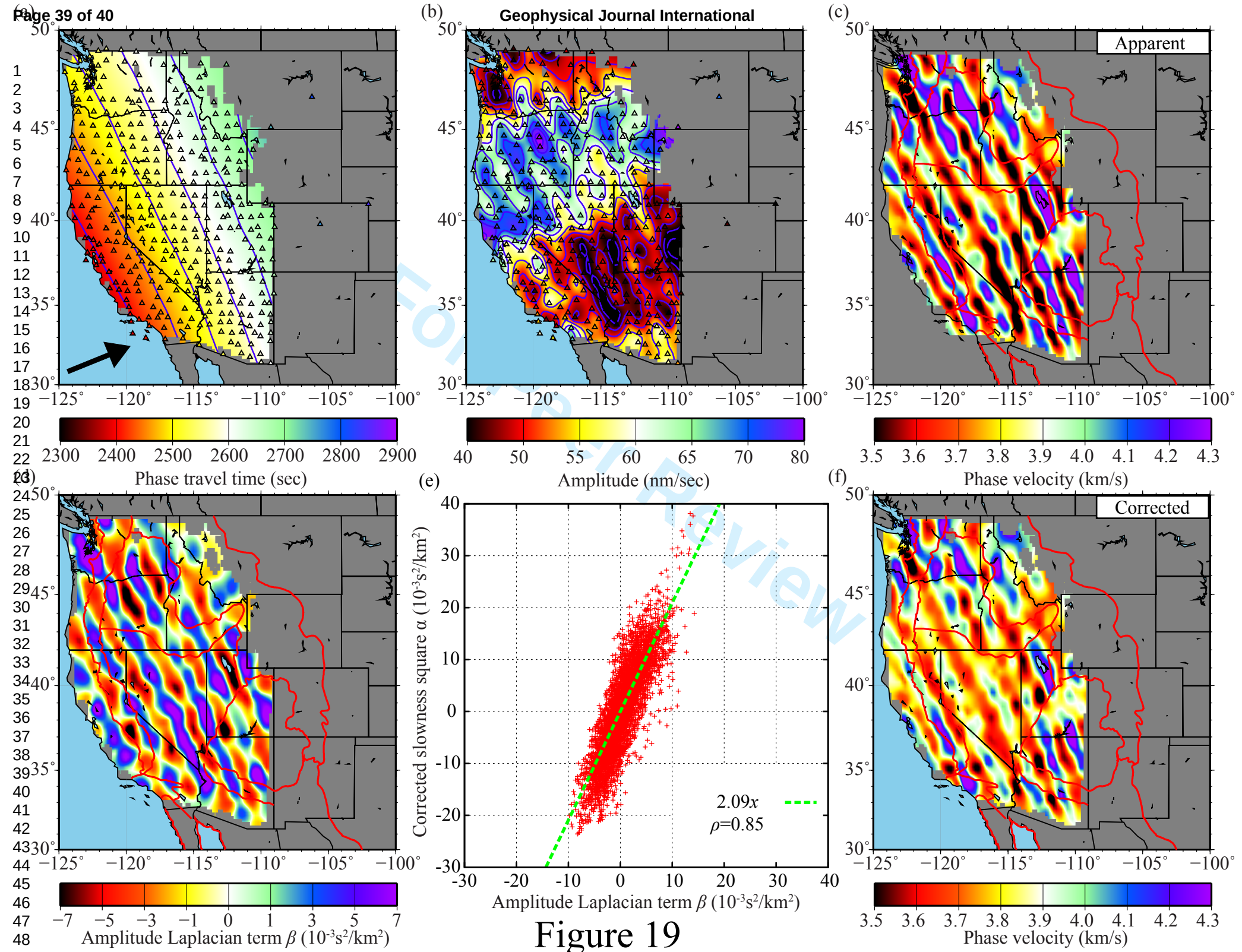

Figure 19

For Peer Review

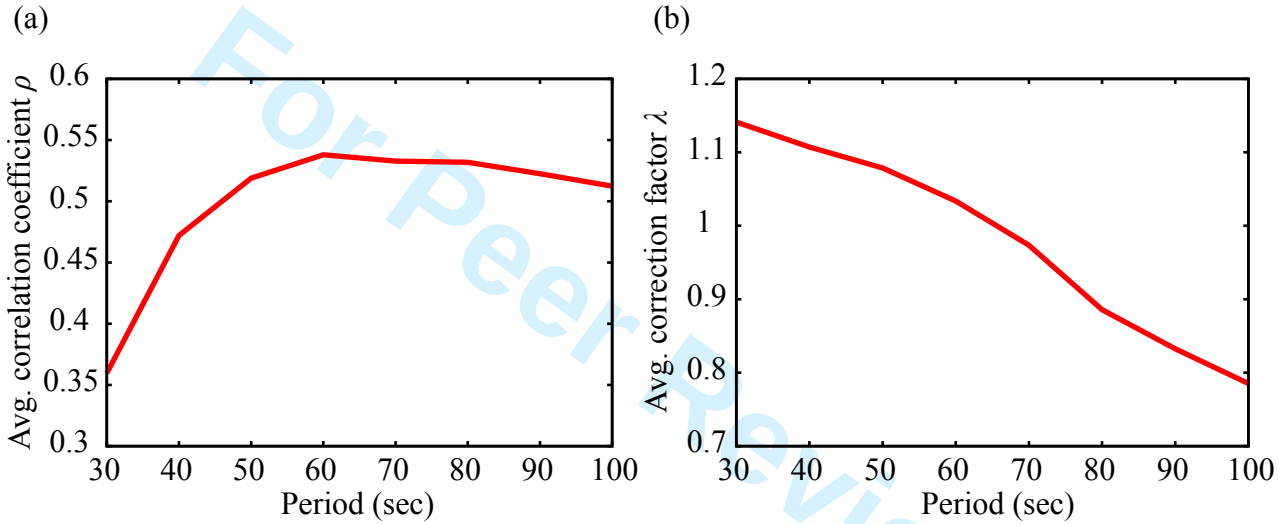

For Peer Review

Figure 20